Journal of
Manufacturing and Materials Processing

MDPI

Article

High-Volume Cement Replacement with Oil Shale Ash and Metakaolin in Pre-Blended Compositions for 3D Printing

Ella Spurina [1], Alise Sapata [1], Genadijs Sahmenko [1,*], Vesna Zalar Serjun [2], Lucija Hanzic [3], Lidija Korat Bensa [3], Evaldas Serelis [4] and Maris Sinka [1]

[1] Institute of Sustainable Building Materials and Engineering Systems, Faculty of Civil and Mechanical Engineering, Riga Technical University, Kipsalas iela 6a, LV-1048 Riga, Latvia; ella.spurina_1@rtu.lv (E.S.); alise.sapata@rtu.lv (A.S.); maris.sinka@rtu.lv (M.S.)
[2] Laboratory for Stone, Aggregate and Recycled Materials, Department of Materials, Slovenian National Building and Civil Engineering Institute (ZAG), Dimičeva ulica 12, SI-1000 Ljubljana, Slovenia; vesna.zalar@zag.si
[3] Laboratory for Concrete, Department of Materials, Slovenian National Building and Civil Engineering Institute (ZAG), Dimičeva ulica 12, SI-1000 Ljubljana, Slovenia; lucija.hanzic@zag.si (L.H.); lidija.korat@zag.si (L.K.B.)
[4] Faculty of Civil Engineering and Architecture, Kaunas University of Technology, Studentu St. 48, LT-51367 Kaunas, Lithuania; evaldas.serelis@ktu.lt
* Correspondence: genadijs.sahmenko@rtu.lv

Abstract

This study presents the development and comprehensive characterisation of a sustainable 3D-printable cementitious composition in which up to 40 wt.% of Portland cement was replaced by a ternary binder containing oil shale ash (OSA) and metakaolin (MK). Following laboratory optimisation, the developed formulations were successfully transferred to industrial production as pre-blended dry mixes at Sakret Latvia Ltd., demonstrating the feasibility of large-scale manufacturing of printable cementitious materials. Attention was devoted to the characterisation of the raw materials and dry mixtures using particle size distribution (PSD), scanning electron microscopy with energy-dispersive spectroscopy (SEM/EDS), and X-ray diffraction (XRD). Two compositions—a reference mixture (REF) and the ternary OSA mixture—were evaluated in terms of printability, mechanical performance, durability, and the influence of the type of sample production. The ternary composition (due to the pozzolanic activity of MK and OSA) exhibited strength development resulting in compressive strength (60.6 MPa) exceeding that of the reference mixture after 90 days of curing (55.3 MPa). Mechanical testing of compression and flexural properties indicated direction-dependent differences between printed and cast specimens. Durability assessment, including capillary water absorption and surface freeze–thaw scaling tests performed using two standardised methods, confirmed frost resistance and the suitability of both mixtures for outdoor applications. The results further indicate that the layered manufacturing process governs moisture transport and direction-dependent mechanical behaviour associated with interlayer interfaces. The developed pre-blended OSA–MK composite represents a promising low-carbon material for industrial 3D concrete printing, combining reduced cement consumption with reliable printability, mechanical performance, and durability.

Keywords: 3D printing; oil shale ash; pozzolanic activity; sustainability; printability; buildability; freeze–thaw cycles

Check for updates

Academic Editors: Mohd Nazri Ahmad and Mohd Rizal Alkahari

Received: 31 July 2026
Revised: 3 September 2026
Accepted: 15 September 2026
Published: 19 September 2026

Copyright: © 2026 by the authors. Licensee MDPI, Basel, Switzerland. This article is an open access article distributed under the terms and conditions of the Creative Commons Attribution (CC BY) license.

1. Introduction

The construction industry is increasingly adopting digital technologies to improve productivity and minimise consumption of material resources. Among these technologies, three-dimensional concrete printing (3DCP) has emerged as a promising additive manufacturing method that enables automated, formwork-free construction directly from digital models. Compared with conventional construction techniques, 3DCP makes it possible to reduce waste, accelerate project delivery, and increase architectural flexibility while supporting the broader digitalisation of the construction sector [1–3].

Despite these advantages, the sustainability of 3DCP remains strongly dependent on the composition and quality of printable cementitious materials [4,5]. Most printable mixtures contain high amounts of Portland cement to ensure adequate pumpability, extrudability, buildability, and early-age strength. However, Portland cement production is responsible for significant energy consumption and CO_2 emissions, motivating the search for alternative binder systems with lower environmental impacts [4,5].

The use of supplementary cementitious materials (SCMs) is considered one of the most effective approaches for reducing cement consumption in concrete. One such alternative material is oil shale ash. This raw material is particularly attractive due to its availability as an industrial by-product and its potential hydraulic and pozzolanic activity. Oil shale ash (OSA) is a large-volume industrial by-product generated during oil shale combustion and pyrolysis processes. Due to its high calcium content and the presence of reactive silicate and aluminate phases, OSA has attracted considerable attention as a supplementary cementitious material and alternative binder in construction applications. Recent studies have demonstrated that the chemical composition of OSA is typically dominated by CaO, SiO_2, Al_2O_3, Fe_2O_3, and MgO, while the proportions of these oxides depend strongly on combustion technology and ash collection location [6]. The authors reported CaO contents ranging from approximately 28 to 38%, combined with significant amounts of reactive silica and alumina, indicating the potential hydraulic and pozzolanic activity of the material [6].

The hydration and hardening mechanisms of OSA differ from those of conventional Portland cement. The hardening process involves hydration of free lime, formation of portlandite, carbonation reactions, hydration of calcium silicates, and precipitation of secondary hydration products such as calcium silicate hydrate (C–S–H), calcium aluminate hydrates (C–A–H) and ettringite ($C_6AS_3H_{32}$) [7]. These reactions contribute to the development of material skeletons. Previous investigations have shown that OSA-based concretes can achieve compressive strengths of more than 25 MPa after 28 days of curing, demonstrating the feasibility of using OSA as a binder component in structural and backfilling applications [7].

A partial replacement of Portland cement with OSA has been investigated by some researchers. Researchers Kalpokaite-Dickuviene et al. reported that the incorporation of oil shale ash significantly affects the hydration kinetics, pore structure development, and durability characteristics of cementitious composites [8]. Although the replacement of cement by OSA may slightly reduce early-age strength, the material promotes long-term hydration and can improve sustainability by reducing clinker consumption.

The binding properties of OSA are closely related to its origination technology and mineralogical composition. Pulverised-firing (PF) ashes generally exhibit hydraulic behaviour due to the presence of calcium silicates and aluminates, whereas circulating fluidised bed (CFB) ashes display predominantly pozzolanic characteristics and higher water demand. Modern combustion technologies have altered the composition of OSA by increasing the content of undecomposed carbonates and reducing the proportion of reactive clinker-like minerals, which may decrease the intrinsic binding capacity of the ash [6].

The latest literature confirms the strong potential of OSA as a regional supplementary binder or filler for 3D-printed concrete composites, particularly in combination with Portland cement, limestone powder, metakaolin, slag or other reactive mineral additions. Materials containing reactive mineral additions are often used to tailor these properties and improve structural stability during printing. Nevertheless, compared with fly ash and slag, direct research on OSA-based 3D printing remains limited. The comparison of samples extracted from 3D-printed elements and conventionally cast samples revealed noticeable differences in mechanical performance. In general, cast samples tend to exhibit higher and more uniform compressive and flexural strengths due to their homogeneous structure and the absence of interfaces formed during layer-by-layer deposition. In contrast, 3D-printed samples contain interlayer boundaries that may act as planes of weakness and promote anisotropic mechanical behaviour [1,9].

Beyond applications in cement compositions, OSA has also been investigated as a precursor for alkali-activated materials and geopolymers (GPs) [10]. The authors discovered the potential of producing GP mortar with OSA and a compressive strength of up to 20 MPa. It was found that dry curing at 60 °C for 24 h provides the best mechanical and durability properties. Research on geopolymer and alkali-activated materials for 3D printing further supports the potential use of OSA in additive manufacturing. Authors Panda et al. [11] demonstrated that geopolymer-based printable materials can achieve adequate buildability and interlayer bond strength and control the fresh-state rheology. Since OSA exhibits chemical characteristics similar to those of high-calcium fly ash, it may be considered a promising component in future 3D-printable binder systems. However, further research is required to evaluate the influence of OSA on 3D-printing open time, structural buildability, interlayer adhesion, and long-term durability of printed elements.

For 3D-printing applications, the variability of OSA composition, particularly particle-size distribution, free lime, sulphate content, and loss on ignition, is especially important because these parameters can influence fresh mix water demand, setting time, structural build-up, interlayer bonding, and durability. This dosage 20 wt.% from cement does not cause a significant reduction in mechanical performance, provided that the mixture is properly proportioned to extrusion and buildability [12].

Other ash-based supplementary cementitious materials have already been more widely studied in 3D concrete printing. Fly ash, ground granulated blast-furnace slag, silica fume, waste glass powder, rice husk ash, biomass ash and municipal solid waste incineration ash have been investigated as partial cement replacements or functional fillers. These materials can improve sustainability and, depending on their fineness and reactivity, can modify rheological properties and mechanical performance. For example, fly ash and ground waste glass have been shown to produce 3D-printable cement pastes with mechanical performance comparable to conventional cement mixtures [13].

When mineral additions such as fly ash, metakaolin, slag, or oil shale ash are incorporated into printable mixtures, their influence on rheology and hydration kinetics further affects interlayer adhesion and mechanical performance. Reactive supplementary cementitious materials can enhance microstructural densification and long-term strength development, although excessive replacement levels may reduce early-age strength and interlayer bond quality [7,8].

Recent reviews emphasise that sustainable 3D concrete printing depends not only on reducing cement content but also on achieving a balance between extrudability, buildability, open time, interlayer adhesion and hardened-state durability. Research authors report 3D-printable, low-carbon one-part geopolymers, their compositions, and the effect of different precursor compositions, activator content, and different admixtures on the fresh and hardened properties of the mixtures [14]. The authors analysed the compressive

strength of one-part geopolymers with cast samples in different directions of printing. The maximum result (61.2 MPa) was reached for mould-cast samples.

The next reviewed study investigated incineration bottom ash (IBA) for the enhancement of sustainability of 3D-printed concrete [15]. The impacts of using IBA to substitute aggregate (0%, 20%, 40%, and 60% by volume) on the fresh properties, hydration kinetics, and hardened properties of 3DPECC were investigated. The results show that the addition of IBA enhanced the degree of hydration; as a result, 3D-printed samples with 20% IBA substitution exhibited improved tensile strength (6.19 MPa), compressive strength (50.47 MPa), and flexural strength (22.60 MPa) compared to those of printed samples without IBA [15].

The reduction in strength observed in printed samples is commonly attributed to imperfect interlayer bonding, moisture loss between deposited layers, and the presence of entrapped air voids generated during the extrusion process. These factors may reduce the continuity of hydration products across adjacent layers and increase porosity, particularly in the interfacial transition zones [1]. Previous studies have shown that the mechanical properties of printed concrete are strongly dependent on printing parameters, including layer height, nozzle travel speed, extrusion rate, and time interval between successive layers [11,16]. The performance of additively manufactured products may also be tailored through post-processing. The research demonstrates a pronounced influence of annealing conditions on the impact toughness of 3D-printed metallic components [17].

Moreover, 3D-printed cementitious materials often exhibit anisotropic behaviour, with lower strength measured in the direction perpendicular to the printing layers compared with the direction parallel to them. Panda et al. reported that the tensile and bond strengths between layers are particularly sensitive to the rheological evolution of the fresh mixture and the degree of surface drying before deposition of the subsequent layer [11]. Similar observations have been reported by [9], who demonstrated that the fresh-state properties required for buildability may simultaneously reduce the ability of successive layers to form a monolithic structure.

Large-scale interlaboratory comparative tests to study the mechanical properties of 3D-printed concrete were conducted within the framework of a technical committee within the international organization RILEM. More than 25 university laboratories participated in the experiments, and the results were summarised in reports [18–20]. The results of cast and 3D-printed samples were compared and tested in different directions. As a result, statistically reliable results were obtained showing the influence of the force application direction on the main mechanical properties of the material. Therefore, differences between cast and 3D-printed samples are primarily associated with the layered manufacturing process rather than the properties of the binder itself. While cast samples generally provide a reference for the maximum achievable material strength, the performance of printed samples is governed by both material composition and process-related factors, particularly interlayer bonding, porosity, and structural inhomogeneity.

Thus, although OSA has been investigated as a supplementary cementitious material, its application in industrially produced pre-blended dry mixes for 3D concrete printing remains insufficiently studied. The present work intends to fill this gap by transferring the laboratory-developed OSA–MK composition with 40 wt.% cement replacement to industrial-scale dry-mix production and subsequently validating its printability, mechanical performance, and durability.

The hypothesis of this study is that a laboratory-developed OSA–MK composition with 40 wt.% Portland cement replacements could be transferred to industrial-scale production as a pre-blended dry mix while maintaining designed composition, suitable printability, mechanical performance, and durability.

The practical goal of this study is to experimentally validate this hypothesis through industrial production and subsequent laboratory tests, including full-scale 3D printing. This work was conducted within the TRANSITION project in collaboration with industrial partner Sakret Latvia Ltd., with a focus on ready-to-use pre-blended dry mixes utilising local raw materials and industrial by-products.

2. Materials and Methods

2.1. Raw Materials

The basic components of the dry mix are Portland cement, OSA, high-reactivity pozzolanic admixture metakaolin (MK), and additives that regulate the setting time of the 3D-printed solution and ensure its stability. Two binder compositions were studied: the reference composition (REF) based on Portland cement and the ternary mix combined on Portland cement, OSA and metakaolin (OSA). The main characteristics of the binding materials used are summarised in Table 1, and the chemical composition is presented in Table 2. The particle microstructure of the samples was analysed by a JEOL IT500 LV (Tokyo, Japan) scanning electron microscope (SEM). The low vacuum mode was employed for analysis, with an accelerating voltage of 20 kV and working distance 10–13 mm. The morphology of mineral components of experimental dry mixes used in this study is shown in Figure 1.

Table 1. Basic mineral components of experimental dry mixes.

	CEM II	OSA	MK	LS
Particle density, g/cm^3	3.13	2.63	2.67	2.73
Moisture content (wt.%)	0.3	0.7	0.0	0.0
PSD: d_{10} (μm)	1.9	2.1	0.7	2.3
d_{50} (μm)	9.7	9.7	6.5	18.5
d_{90} (μm)	28	39	50.2	176
Specific surface area (m^2 g^{-1})	1.3324	1.3105	15.6109	2.4446

In this research, composite Portland Cement CEM II 42.5 A/LL R in accordance with EN 197-1:2011 [21] was used as a main binding compound (CEM II). Portland cement is produced by Schwenk Ltd. (Broceni, Latvia). In accordance with the standard [21], in this type of cement up to 20% clinker is replaced with limestone filler; this makes cement more environmentally friendly by significantly reducing the amount of clinker and, consequently, carbon dioxide emissions. In accordance with the producer's EPD declaration, this cement released 659 kg of CO_2 (GWP total), compared to 706 kg of CO_2 for CEM I 42.5 R. Limestone powder was also used as an inert filler. This component does not participate in the chemical reactions of cement hydration and can be considered as a mineral additive that improves the particle granulometry at the micro-level and controls the rheological properties of the 3D-printable mixture [22].

Table 2. Binding material chemical composition.

	SiO_2	Al_2O_3	Fe_2O_3	CaO	MgO	SO_3	Na_2O	K_2O	TiO_2	P_2O_5	LOI
CEM II	21.8	5.8	3.6	58.6	3.1	2.0	0.30	0.8	0.2	0.1	3.40
MK	50.2	42.7	1.5	0.4	0.5	0.13	-	0.3	1.4	0.1	2.70
OSA	21.5	5.6	2.9	35.6	3.0	17.3	0.4	2.9	0.3	0.1	9.6
LS	2.6	2.2	0.4	49.8	1.8	0.1	0.4	0.3	-	-	42.1

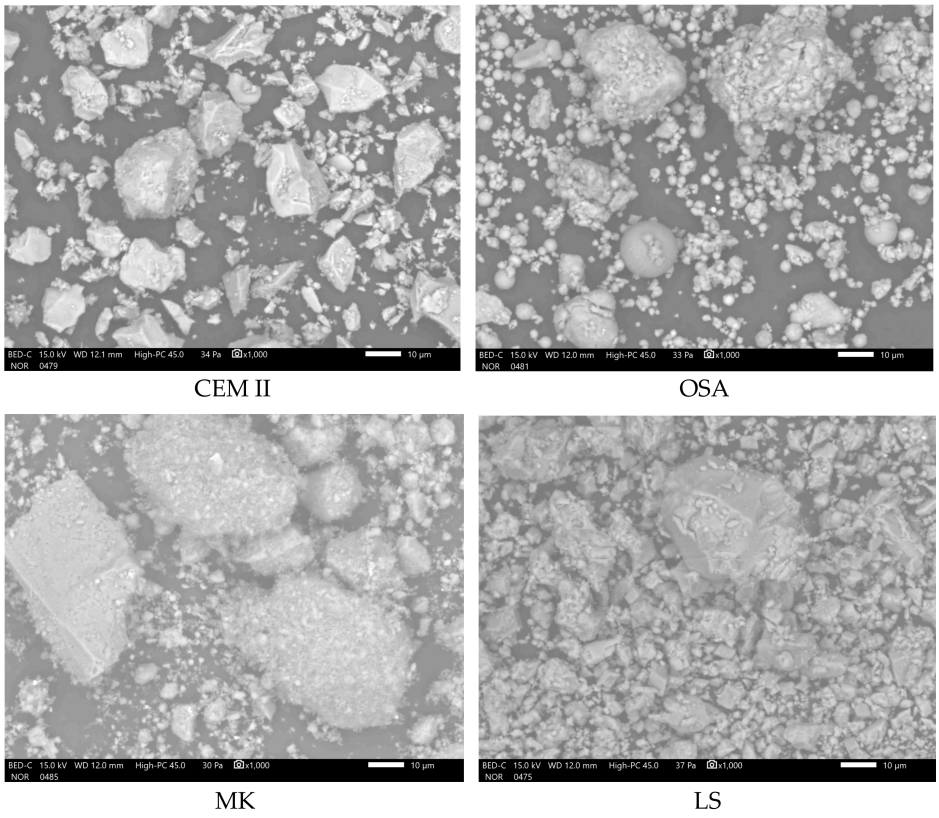


Figure 1. Particle morphology (CEM II, OSA, MK, and LS).

As industrial waste, OSA was used as the main cement replacing material. OSA was collected from Eesti Elektrijaam (Vaivara, Estonia) and extracted from the flue gas stream using a novel integrated desulphurizer (NID). According to the obtained micro-images and analysis results reported in Hanzic et al. [23], this ash is characterised by high CaO and SiO_2 contents. The OSA particle density is 2.6 g/cm^3, which is less than that of Portland cement but corresponds to the density of inert filler and limestone (Table 1). Regarding morphology investigation (Figure 1), it is observed that particles of cement, limestone, and metakaolin are mostly angular-shaped, while OSA contains some highly spherical microparticles, which is not observed in the case of cement.

The OSA type used in this study was selected based on previous investigations comparing oil shale fly ashes and bottom ashes originating from different combustion processes. Among the evaluated materials, OSA-NID (novel integrated desulphurization) fly ash showed the most suitable characteristics for the developed 3D-printable compositions and was therefore selected for further investigation [23].

Previous characterisation of the selected OSA-Ees(nid) showed a free CaO content of 4.5 wt.% and a Le Chatelier soundness expansion of 3.6 mm [23]. The total SO_3 content determined by XRF was 17.3 wt.%; however, soluble sulphate content was not determined separately. Therefore, its contribution to possible long-term expansive reactions cannot be quantified directly and should be addressed in further studies.

Highly reactive metakaolin was used as an active pozzolanic additive, ensuring the binding of free lime to form additional C–S–H and C–A–H hydration products. In this study, metakaolin Astra MK-40 (Astra Polska Ltd., Sękocin Stary, Poland) was used as a commercial material for concrete production. Metakaolin is commonly used as a supplementary cementitious material (SCM), replacing about 5–20% of Portland cement by mass, depending on performance requirements [24]. MK was produced by the dehydration

of a kaolin clay mineral ($Al_2(OH)_4Si_2O_5$) into an amorphous dehydrated state after thermal treatment at 700–800 °C.

Limestone powder (produced by Satini-LM Ltd., Latvia) is a finely ground inert micro-filler which, together with sand, provides the required granulometric distribution with a controlled volume of fine particles which are necessary for the fresh mix stability and extrudability. Normally, limestone powder as a part of the cement paste shows minor influence on hydration processes [25]. Medium-sized sand of 0/2 mm was used as an inert filler. The sand was supplied by Sakret Ltd. (Rumbula, Latvia). Most of the sand consists of quartz particles and has a wide range of particles from 0.1 to 2 mm.

The particle density was highest for CEM II (3.13 g/cm^3), while the values for OSA, MK, and LS were relatively similar, ranging from 2.63 to 2.73 g/cm^3. MK had the smallest median particle size (d_{50} = 6.5 µm) and the highest BET specific surface area (15.61 m^2 g^{-1}) among the investigated constituents. The comparatively high d_{90} value of MK (50.2 µm), despite its low median particle size, may indicate the presence of some coarser agglomerates that were not fully dispersed under the selected laser-diffraction measurement conditions. CEM II, OSA, and LS exhibited substantially lower specific surface areas. LS was the coarsest powder, with d_{50} = 18.5 µm and d_{90} = 176 µm, indicating a broad particle-size distribution and lower overall fineness despite its moderate specific surface area of 2.44 m^2 g^{-1}.

The complex admixtures and micro-fibres were already incorporated into dry mix composition to control the characteristics of 3D-printed concrete during different stages of the printing process. The admixtures include superplasticizer (SP), air-entraining agent (AEA), viscosity-modifying additive (VMA), and polypropylene micro-fibre (PP) in the amount of 0.05 wt.% with a diameter of 22 µm and length of 6 mm.

SP was added to decrease internal friction in concrete mix by dispersing the binder particles [26,27]. AEA is normally added to a concrete mix to improve frost resistance. Air-entraining additive creates microscopic air bubbles that absorb the expansion of pore water during freezing and thus prevent the destruction of the material structure [28]. In the case of 3D printing, it becomes possible to use the additional function of an air-entraining admixture, which provides a stabilising effect and prevents mix bleeding and separation of the cement paste on the surface [29].

A viscosity-modifying additive (VMA), in the case of 3D printing, increases the structural bond between particles, ensuring stability. Its mechanism of action lies in the water-holding capacity of micro-cellulose and the creation of a system resistant to separation due to the increase in internal cohesion of the mixture.

The chemical composition of the individual components of the binder is shown in Table 2. According to the data obtained, the chemical composition of Portland cement CEM II is characterised by a high CaO content (58.6%) and moderate amounts of SiO_2 (21.8%) and Al_2O_3 (5.8%). Metakaolin is composed of 50.2% SiO_2 and 42.7% Al_2O_3, and it mostly consists of an amorphous phase, which is the reason for its highly reactive properties.

Particular attention should be paid to the oil shale ash (OSA), which contains significant amounts of CaO (35.6%), SiO_2 (21.5%), and Al_2O_3 (5.6%), indicating the content of both alkaline and acidic oxides. In addition, OSA exhibits a relatively high SO_3 content (17.3%), substantially higher than that of the other constituents. The increased sulphate content is associated with the industrial combustion process, during which sulphur compounds present in the oil shale are oxidised and subsequently incorporated into the ash as sulphate-bearing phases. The presence of SO_3 may influence the hydration process, setting behaviour, and formation of sulphate-containing hydration products. Furthermore, OSA contains moderate amounts of MgO (4.6%) and alkali oxides (Na_2O and K_2O), which may also affect the reactivity of the blended binder.

Limestone powder (LS) is mainly a calcareous filler, characterised by high CaO content (49.8%) and a high loss on ignition (42.1%), reflecting its predominantly carbonate nature. The combination of calcium-rich cement and limestone powder with reactive metakaolin and sulphate-containing oil shale ash provides a chemically diverse system capable of promoting both hydraulic and pozzolanic reactions, potentially enhancing the microstructure and long-term performance of the blended cementitious material.

To obtain a more in-depth understanding of the chemical and mineralogical composition, a semi-quantitative analysis was performed on prepared samples of mineral components. The objective of the semi-quantitative analysis was to establish the proportion of the amorphous phase, which represents the pozzolanic phase. The representative portion of each material subsample (defined by quartering procedure) was ground in an agate mortar to a particle size of <63 µm. The test portion was placed into a 27 mm diameter sample holder.

The phase composition analysis was performed by powder X-ray diffraction (XRD) using the Panalytical Malvern Empyrean (The Netherlands) diffractometer with Cu–Kα radiation. The measurements were carried out at 45 kV voltage and 40 mA current. Data were collected over the 2θ range from 5° to 70°. The increment measurement time was 150 s. The samples were prepared for X-ray diffraction (XRD) analysis using 27 mm diameter sample holders and the back-filling method. XRD charts are presented in Figure 2.

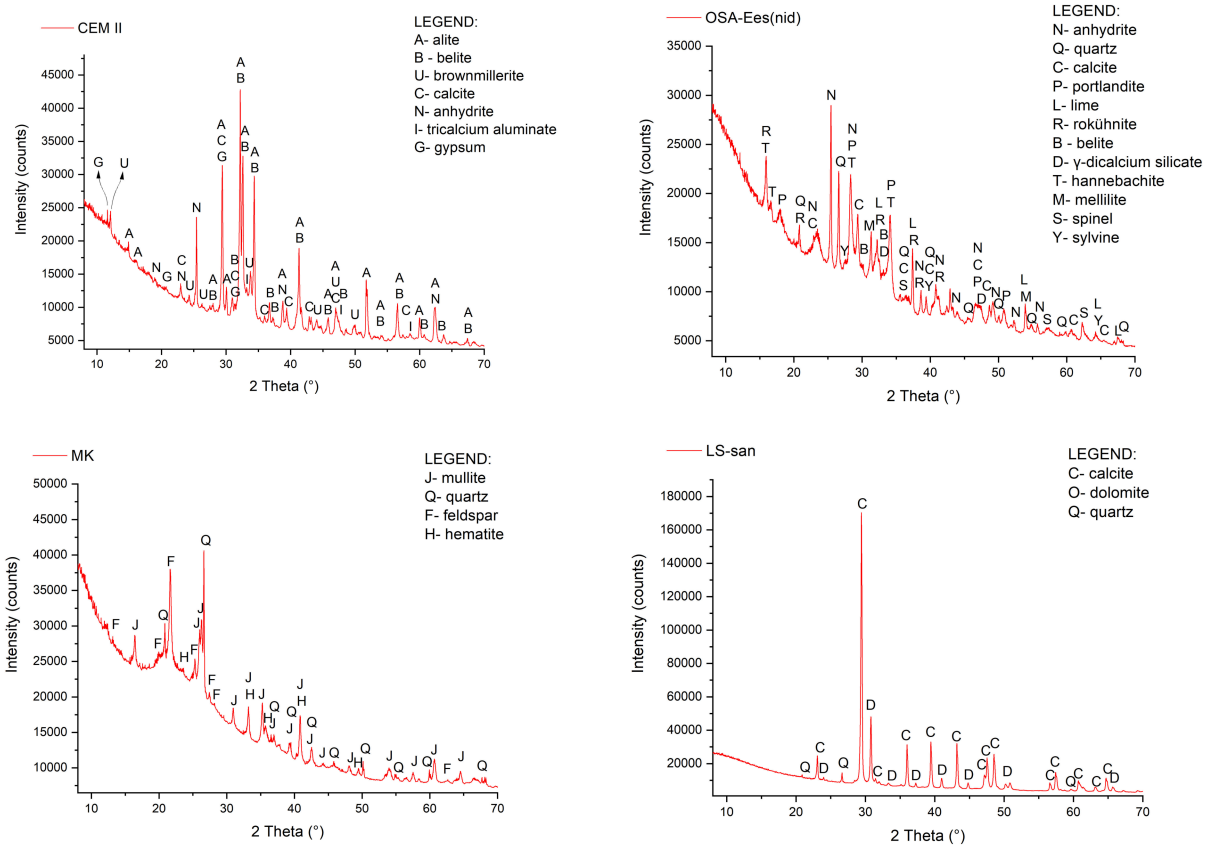


Figure 2. XRD semi-quantitative analysis of mineral components of experimental dry mixes (CEM II, OSA, MK, and LS).

The results were analysed with Panalytical Highscore 4.8 diffraction software using the ICDD Powder Diffraction File PDF-4+ database as a source of references for the crystalline phases. The quantitative XRD analysis (QXRD) was performed by using an external standard procedure and the Rietveld refinement approach.

The results of the qualitative XRD analysis showed that CEM II is composed of common clinker phases, namely alite, belite, brownmillerite, and tricalcium aluminate. Typical sulphate phases of cement, gypsum and anhydrite were also identified. The presence of calcite confirms that the investigated CEM II is a composite cement containing limestone, which was added according to the producer's specifications.

The LS micro-filler is composed predominantly of calcite, with dolomite identified as a minor phase and quartz as a trace phase.

The diffractogram of the metakaolin sample exhibits a typical broad amorphous hump in the range of 18–28° 2θ, indicating a high proportion of amorphous fraction. The identified crystalline phases, including mullite, quartz, feldspar, and hematite, are present only as minor constituents. QXRD of OSA (sample OSA-Ees(nid)) showed that amorphous fraction accounts for 60.2%. The most abundant crystalline phases present account for calcareous phases, calcite (6.4%) and portlandite (6.33%), followed by anhydrite. Sulphate-bearing phases present account for 10.72% (anhydrite 6.19% and hannebachite 4.53%). Quartz accounts for 4.8%. The following are dicalcium silicates: the well-known larnite–clinker composite phase, at a quantity of 3.13%, and its non-hydraulic form, gamma dicalcium silicate polymorph, at a quantity of 4.25%. The following are the calcium oxide–lime (2.59%) phases present in traces or in quantities below 1%: chloride-bearing phases (rokuhnite and sylvine) and spinel mineral phases.

2.2. Mix Compositions

Two basic compositions were developed through previous iterations, taking into account the physical and mechanical properties and the possibility of 3D printing [30]. The proportions of the mixture were selected based on the granulometric composition and also ensuring the necessary paste content by introducing limestone micro-filler, as well as stabilising, plasticizing, and air-entraining admixtures and polypropylene micro-fibres (L = 6 mm) for structuring the fresh mix.

The chemical origination of methyl-cellulose (MC) admixtures used for stabilising concrete mixes stems from the etherification of natural cellulose molecules. The used polycarboxylate superplasticizer is a comb-shaped polymer. Air-entraining admixture is composed of anionic surfactants (surface-active agents) that lower the surface tension of water and stabilise microscopic air bubbles during mixing.

The developed composition was expanded to a production scale as a result of cooperation with the company Sakret Latvia ("Ritvari", Rumbula, Latvia). Two types of dry, pre-mixed compositions were adopted for production in industrial conditions.

The component proportions of these two basic compositions are summarised in Table 3. The reference binder in the REF composition is Portland cement, and the OSA composition is a ternary mix of Portland cement, oil shale ash and metakaolin.

Table 3. Basic mix compositions.

Mix Name	CEM II	OSA	MK	LS	AEA	SP	VMA	Sand	Fibre	Sum, g
Dry composition, g per 1 kg of dry mix										
REF	333	-	-	83.1	0.05	1.66	0.03	582	0.50	1000
OSA	200	83.1	49.9	83.1	0.05	1.66	0.03	582	0.50	1000
Dry composition, parts related to cement										
REF	1.00	-	-	0.25	0.0001	0.0050	0.0001	1.75	0.0015	3.00
OSA	0.60	0.25	0.15	0.25	0.0001	0.0050	0.0001	1.75	0.0015	3.00

The amount of water in the mixture was selected to ensure the necessary extrudability and buildability for 3D printing. For both mixtures, the amount of water added was 15% of

the mass of all dry components. In the reference mix, water–binder ratio is determined as a relation W/CEM II but in ternary composition as a relation W/(CEM II + OSA + MK). The water–binder ratio was provided as 0.45 in both compositions.

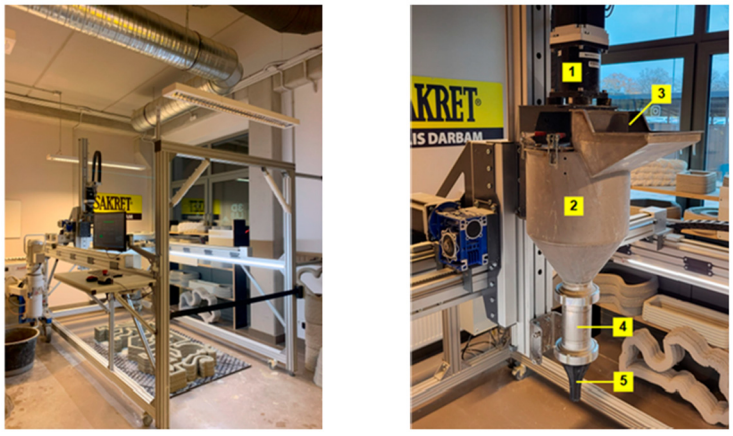
2.3. Mixing, Fresh Properties Testing, and 3D Printing

The mixtures were prepared for the experiments during 3D printing, and samples were produced for further testing on mechanical properties and durability. A laboratory pan-type forced-action mixer M50 (Filamos s.r.o., Příbram, Czech Republic, useful volume 37 dm^3) was used to prepare the 3D-printed composition. Each batch was prepared following the same procedure. The dry mixture was dosed into the mixer, and water was gradually added while mixing at a speed of 60 min^{-1} for 180 s, allowing the mixture to rest for 10 min, and then remixing for an additional 60 s with a mixing speed of 60 min^{-1}. The prepared mix was then manually loaded into the hopper of the 3D printer.

Fresh-state mix properties were determined using standard and non-standard methods [31]. Workability was evaluated using the cone flow method according to EN 1015-3 [31]. The essence of the method consists in measuring the spread diameter after 15 jolts of a cast cone of fresh mixture. Based on preliminary printing trials, an optimal flow diameter in the range of 160–180 mm was identified as suitable for extrusion-based 3D printing.

In this study, open printing time was evaluated indirectly from the flow spread test. Therefore, it should be considered a practical process-related indicator rather than a complete rheological characterisation of the printable time window.

Experimental 3D printing was adopted using a custom-made gantry-type printer developed at the 3D Concrete Printing Laboratory, Faculty of Civil and Mechanical Engineering, Riga Technical University (Figure 3) [32]. The printer is controlled by a computer that has three degrees of freedom, and the allowed printing area is 1000 × 1000 × 1500 mm. Printing was performed using a batch-fed, auger-driven extrusion system, a circular nozzle with a diameter of 36 mm was used for sample printing, and a 25 mm nozzle was used for the slug test. The nozzle standoff distance was maintained at approximately 10 mm. The extrusion rate varied between 1.5 and 5 L/min, whereas the nozzle travel speed ranged from 10 to 60 mm/s. The deposited filaments exhibited a width of approximately 40–50 mm, depending on the fresh-state behaviour and mix buildability.



(a) (b)

Figure 3. Custom-made laboratory concrete printer at RTU: (**a**) printer setup with the aluminium frame and print area; (**b**) gantry system closeup: (1) motor; (2) hopper; (3) inlet; (4) pipe; (5) nozzle.

3D-printed elements and cast samples were covered with plastic film after producing. During the 3D-printing process, the basic fresh-state properties were evaluated, including the fresh mix density, yield stress, cone spread, and buildability.

The plastic yield stress of the fresh mixture was determined using the slug test method [33]. The yield stress (τ_c) was calculated based on the mass of the extruded material according to the following equation:

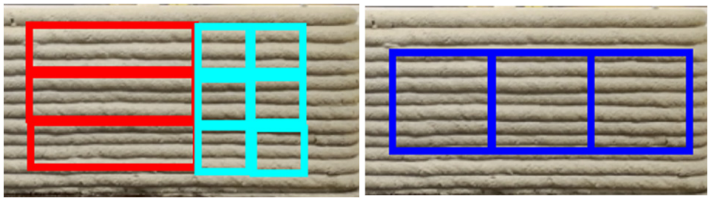
$$\tau_c = \frac{g \times m_s}{\sqrt[2]{3} \times S} \quad (1)$$

where $S = \pi R^2$ is the nozzle cross-sectional area, R is the nozzle radius, g is gravitational acceleration, $m_s = \rho S L_s$ is the slug mass, L_s is the slug length, and ρ is the fresh density of the extruded mixture. The yield stress reported later is the arithmetic mean of three measurements on the test sample.

Buildability was evaluated using a buckling test to determine the maximum number of layers that could be successfully printed before the structural instability or structural collapse of the freshly printed element. The buildability test is a practical indicator of both extrusion stability and structural integrity during printing.

2.4. Sample Preparation and Testing

In this study, small-sized prism samples of 40 × 40 × 160 mm were used for testing mechanical properties. Two types of samples were prepared from each composition: the samples that were directly cast into the mould after mixing, as well as samples that were cut from a 3D-printed element. For these purposes, a 3D-printed element with dimensions of 650 × 330 × 400 mm was specially created, and a round nozzle with a diameter of 36 mm was used to achieve the desired filament width. Three days before testing, the samples were cut out from the printed element using a diamond disk saw: prismatic samples of 40 × 40 × 160 mm for the mechanical test, cubes of 40 × 40 × 40 mm for the water absorption test, and plates of 100 × 100 × 50 mm for the frost resistance test. The sampling scheme is explained in Figure 4.



(**a**) (**b**)

Figure 4. Sampling scheme from a 3D-printed element: (**a**) red—prisms for the mechanical test; light blue—cubes for the water absorption test; (**b**) blue—plates for the frost resistance test.

Both cast and 3D-printed samples after production were covered with plastic sheets to prevent moisture loss. Cast samples were demoulded after 24–48 h and cured at 21 ± 1 °C and a relative humidity (RH) > 95% until the age of testing. 3D-printed elements were also stored in similar humid climate conditions.

Flexural and compressive strength. The placement of samples and the direction of load application during testing in relation to the 3D-printing direction are shown in Figure 5. Before testing, the samples were weighed and measured to determine density. Compressive and flexural strength were determined using a universal testing machine Zwick Z100 (ZwickRoell GmbH & Co., Ulm, Germany) in accordance with EN 196-1 [34]. When conducting the bending test, the distance between the supports was 100 mm. The loading rate was 50 ± 10 N/s for the flexural test and 2400 ± 200 N/s for the compressive test. Strength was calculated and measured in MPa.

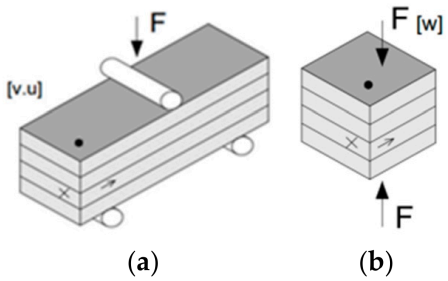


Figure 5. Mechanical testing scheme related to casting direction: (**a**) flexural test; (**b**) compression test.

Statistical differences between mechanical test results were evaluated using two-sided Welch's *t*-tests, which do not assume equal variances between groups. Statistical significance was defined as $p < 0.05$. Sample testing results are reported as mean ± standard deviation. To determine the bending strength, three samples were used per series, and for the compressive strength, five samples were used, respectively.

Water absorption and frost resistance testing were carried out in accordance with RILEM TC 304-ADC [35]. In cold and humid climates, the durability of cementitious compositions is associated with the effect of alternating exposure to moisture and freeze–thaw cycles.

At the age of 28 days, five samples per test series (printed series and mould-cast series) were dried in an oven at 40 °C until constant mass. Afterwards, four of the six element sides were coated with two layers of epoxy to ensure unidirectional water ingress. In case of mould-cast samples, one of the casting sides acted as an exposure surface (this was left uncoated together with the opposite surface). In case of printed samples, the vertical side of 3D-printed elements acted as an exposure surface (submerged in water). The inner and outer printed surfaces of the printed object remained uncoated.

Before water exposure, the nominal dimensions and the initial dry mass were determined to measure the weight of the epoxy coating. Thereafter, samples were placed on two line supports (intended diameter or side length of the supports equalling 2 mm) in sealed conditions to avoid evaporation during the absorption tests. The line supports were placed transverse to the print direction. Due to the curvature of the printed surface and to ensure a similar water level, the submersion level for all test series was 5 ± 2 mm above the top of the line supports, as shown in Figure 6.

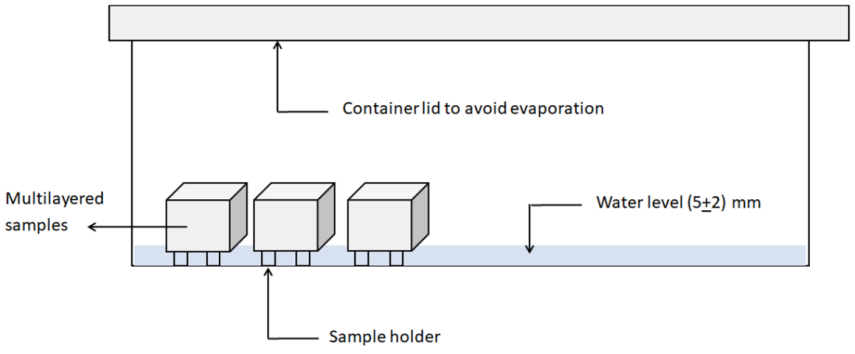


Figure 6. Capillary water absorption test in accordance with RILEM TC [35].

The water uptake into the cementitious materials needs to be determined by weighing the samples at predefined time intervals (1, 3, 7, 15, 30, and 60 min and every hour up to 6 h after water contact). After this first period, samples were weighed again after 24 and 144 h. Before every measurement, samples were taken out of the container and wiped carefully with a wet cloth to remove the surplus water. Thereafter, they were immediately returned

to the supports in the container. The results are depicted as absorption curves (kg/m^2) in function of the square root of time.

Freeze–thaw resistance was evaluated according to LVS CEN/TS 12390-9 (slab test method). Adaptations include the use of prismatic plate samples with dimensions of 100 × 100 × 50 mm instead of standard scaling samples 150 × 150 × 50 mm and the use of plastic containers rather than standard steel containers. The test surface (facade side of 3DP element) was exposed to freeze–thaw cycles, while the side surfaces were sealed to prevent penetration of the test liquid, and remaining surfaces were thermally insulated. A 3 mm layer of 3% NaCl solution was placed on the exposed surface and covered with a polyethylene sheet to avoid evaporation. The samples were subjected to repeated freeze–thaw cycles between positive and negative temperatures in the range −20/+20 °C. Two methods of cyclic freezing were used: the standard method, which performs one cycle per day, and the accelerated method, which performs two cycles per day (Figure 7). Surface scaling was evaluated after 14, 28 and 56 cycles, by expressing the cumulative scaled mass relative to the exposed surface area, in kg/m^2. Five samples (for each set) were used for water absorption and frost resistance tests.

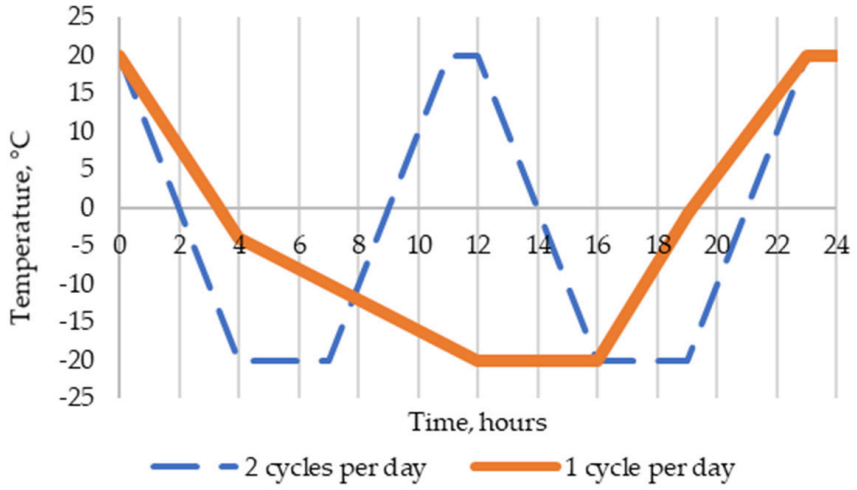


Figure 7. Freeze–thaw resistance temperature chart.

3. Results and Discussion

3.1. The Properties of Pre-Blended Dry Product

Taking into account the mix proportions developed in the laboratory, industrial pre-blended dry mixes for 3D printing were produced in Sakret Latvija Ltd. The materials were packed in standard 25 kg bags and delivered to the laboratory for testing and 3D-printing experiments. Two types of mixes were prepared: REF and OSA.

To assess the actual granulometric composition, the samples of both mixtures were tested using the laser diffraction method. The PSD test was carried out in compliance with standard ISO 13320:2020 [36] using the Microtrac SYNC 5001 instrument. The charts of the granulometric composition are graphically presented in Figure 8. The results indicate that for both mixes the particle size distribution curve is a balanced line, including a wide range of particles from 1 µm to 2 mm. The lower limit of 1 µm corresponds to the binder microparticles, and with that, the upper limit of 2 mm corresponds to the maximum size of sand used as an inert filler. Comparing the granulometric composition of both mixes, the percentage difference does not exceed 6%. The particle size distribution of OSA demonstrates a slightly finer mix compared to the REF composition. This can be explained by the fact that 40% of the cement is replaced with a combination of OSA and MK, which is characterised by finer microparticles (in accordance with Table 1).

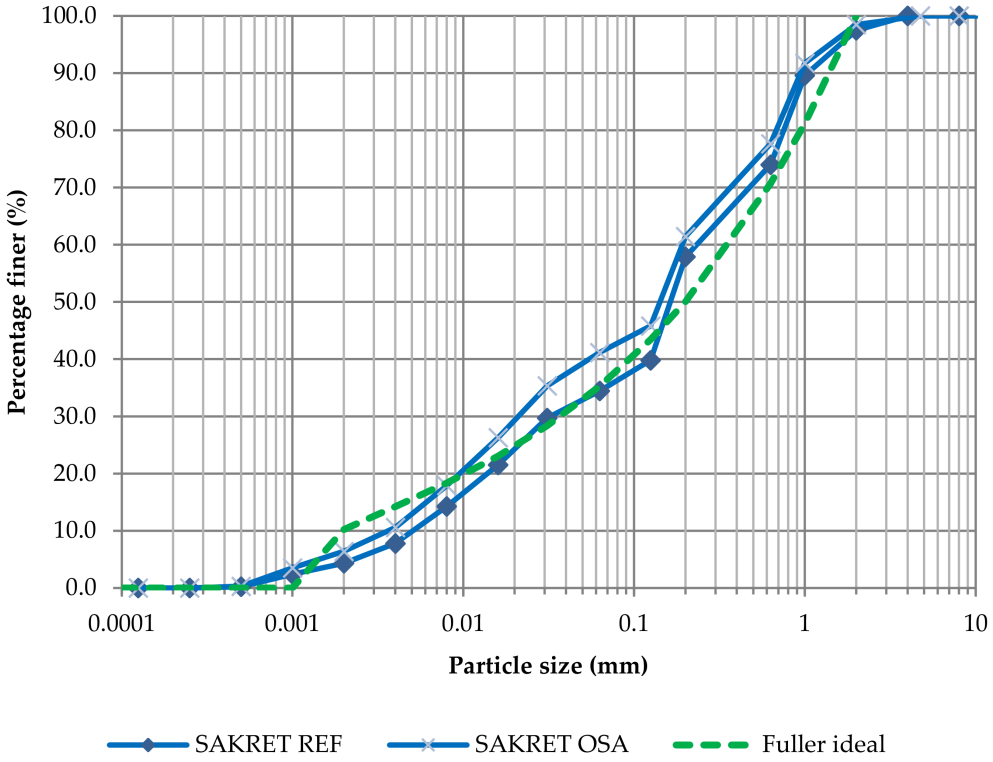


Figure 8. Pre-blended product particle size distribution.

To characterise the particle size distribution and quality of particle packing in a multi-component mix, various models of optimal packing of multi-fractional aggregate are practically used. The most convenient approach is the ideal granulometric curves, which can be described by a simple mathematical equation. For example, in this case, a modified Fuller–Thompson model [37] in accordance with the following formula:

$$P_{\mathrm{i}} = 100\ ((x_i - D_0)/D)^n \quad (2)$$

where P_i is the percentage passing, x_i is the particle size (mm), D is the maximal particle size in the aggregate (mm), D_0 is the initial point of an "ideal" curve (minimal particle size), and n is the degree of the mathematical equation.

The critical indicator is the maximum aggregate size D, which depends on the nozzle diameter, and the degree of the equation n, which determines the ratio between fine and coarse fractions. In this case, using the previous practical experience in RTU 3D laboratory [38] and the experience of other researchers summarised in scientific publications, the following parameters of the Fuller–Thompson curve were used: n = 0.30, D = 2.0 and D_0 = 0.001 mm. The corresponding ideal curve is indicated by the green line in Figure 8.

It should be mentioned that the limited number of optimised compositions does not allow a statistically meaningful quantitative correlation between PSD and rheological parameters. Such behaviour is also influenced by different interacting factors, such as binder chemistry, water content, admixtures and hydration kinetics.

The mineralogical composition of dry pre-blended mixes (REF and OSA) is summarised in Figure 9.

The results of the XRD analysis show that the most abundant phases are quartz, feldspar, and carbonate (dolomite), representing the phases from the coarse aggregate fraction. This is followed by calcite from LS sand and cement and further by the cement phases alite and belite, together with minor sulphate phases (anhydrite and gypsum) originating from the cement and OSA raw materials. It should be stressed that the XRD

analysis of the finished pre-blended products was performed as a semi-quantitative analysis. Therefore, the results confirm the presence of the expected crystalline phases but do not provide their exact quantitative phase proportions.

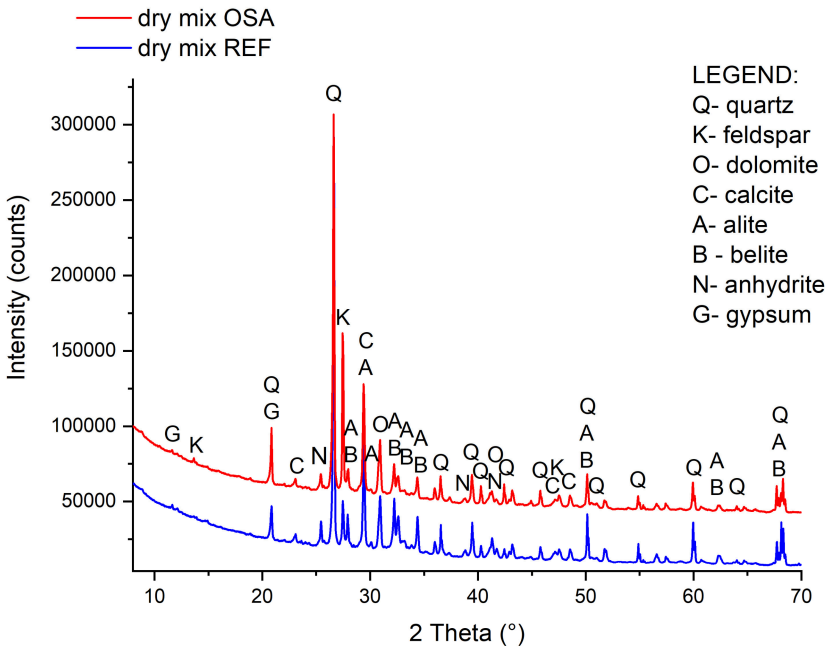


Figure 9. Pre-blended product XRD chart.

To obtain an objective picture of the formation of the material structure when replacing 40% of the cement clinker, XRD tests were additionally carried out on hardened samples aged 90 days. Based on the semi-quantitative analysis (Figure 10), the main observations are as follows:

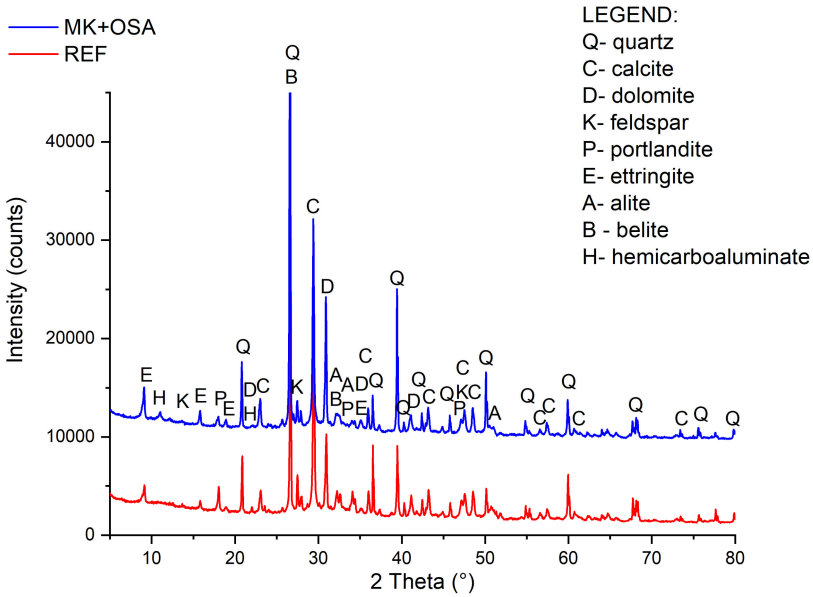


Figure 10. Hardened compositions XRD chart.

Alite and belite: Somewhat higher amounts are observed in REF compared with OSA composition. This could indicate enhanced hydration in the systems containing SCMs, possibly due to the additional nucleation sites provided by the SCMs.

Portlandite: The amount of portlandite is higher in REF than in OSA. The lower portlandite content could be related to its consumption through the reaction of the SCMs.

Ettringite: Higher amounts are observed in OSA than in REF. This could be related to the additional sulphate introduced with OSA, in which anhydrite is present in relatively high amounts.

Monocarboaluminate: Monocarboaluminate is not detected in REF, whereas it is formed in OSA. This indicates the formation of an additional AFm phase in the SCM-containing systems.

3.2. Fresh Mix Characterisation and 3D-Printing Properties

Full-scale 3D-printing experiments were conducted using an RTU concrete 3D printer for both developed compositions of REF and OSA. Open print time was provided for at least 40 min for both compositions. To ensure the statistical reliability of the results, each composition was tested at least four times with provided mixing on different days. Each single-mix experiment included a cone flow test (at 10–15 and 40–45 min), determination of the fresh mix density, three attempts at slug tests and one buildability test. The last-mentioned test was performed only once due to the duration of the experiment and the risk of changing the properties of the mixture. Based on the results of the slug test, the yield stress was determined using Formula (1), depending on the number and mass of the slugs and the nozzle diameter. The results of fresh mix properties are summarised in Table 4. Air content is the most sensitive parameter for control; in all batches, it was maintained in a range from 9.8 to 12.5%. In general, both REF and OSA compositions have minor differences visually and in technical characteristics. The line width in both cases is maintained close to 44 mm, which indicates similar rheological properties during extrusion.

Table 4. Fresh mix properties and buildability characteristics.

	REF	**OSA**
Nozzle diameter, mm	25	25
Slug mass. g/1 piece	190–287	208–265
Line width, mm	44.5 ± 10	43.8 ± 10
Flow diameter at 10–15 min, mm	175 ± 19.8	161 ± 11.1
Flow diameter at 45 min, mm	160 ± 12.9	157 ± 7.5
Air content, %	9.8–12.5	10.0–12.0

The slug test provides an extrusion-relevant estimate of plastic yield stress. It should be noted that independent rotational-rheometer measurements were not performed in the present study, and rheological measurements of related GCP compositions using rotational rheometry were reported in our previous work [30]. Further systematic correlation between rheometer-based and extrusion-based yield-stress measurements will be addressed in future studies.

The most distinctive feature of the two compositions is the time-depending change in cone spread (flow diameter). In the case of the reference composition, after 45 min there is a significant reduction in cone spread from 175 to 160 mm, a difference of 15 mm. In the case of the OSA composition, this change is from 161 to 157 mm, a difference of 4 mm. High retardation of workability of the OSA composition can be explained by the low content of active hydraulic binder clinker Portland cement. Other researchers also note an increase in setting time and a slowdown in hydration processes when replacing cement with oil shale ash [39].

The results for yield stress (by slug test) and buildability test are summarised in Figure 11. The results show that both compositions exhibited comparable 3D-printing performance. The REF mixture had a slightly higher average yield stress (3008 Pa) than the

OSA mixture (2866 Pa), indicating a marginally greater resistance to deformation. However, the buildability results were almost identical, with both mixtures supporting approximately 33 printed layers before buckling (33.1 for REF and 32.9 for OSA). These results indicate that replacing part of the cement with oil shale ash had only a minor effect on the fresh-state mechanical properties and did not significantly reduce the buildability of the printed elements. In both cases, the dispersion of the results overlaps, so it can be assumed that both compositions have statistically identical values of yield stress and buildability.

Figures 12 and 13 illustrate the typical failure mode of the printed cylinders for both REF and OSA compositions. In all tests, failure occurred progressively rather than suddenly. As the number of deposited layers increased, the lower layers experienced gradual compression and lateral deformation, leading to buckling of the cylinder wall and the eventual collapse of the sample. No noticeable differences in the failure mechanism were observed between the two compositions, indicating that the incorporation of oil shale ash did not alter the structural stability of the printed elements. The OSA samples exhibited a failure pattern and deformation behaviour comparable to the reference mixture, confirming similar buildability characteristics.

The measured yield stress values (2866–3008 Pa) and the buildability of approximately 33 printed layers are consistent with values reported for printable cementitious materials in the literature [40]. Previous studies have demonstrated that successful extrusion-based 3D printing requires sufficient green yield stress to resist the increasing self-weight of the deposited layers while maintaining adequate extrudability. Plastic collapse and buckling of the lower layers are recognised as the dominant failure mechanisms governing buildability, which agrees well with the failure mode observed in the present study. The similar yield stress and buildability results obtained for the REF and OSA mixtures therefore indicate that the partial replacement of Portland cement with oil shale ash does not adversely affect the fresh-state mechanical stability of the printed elements.

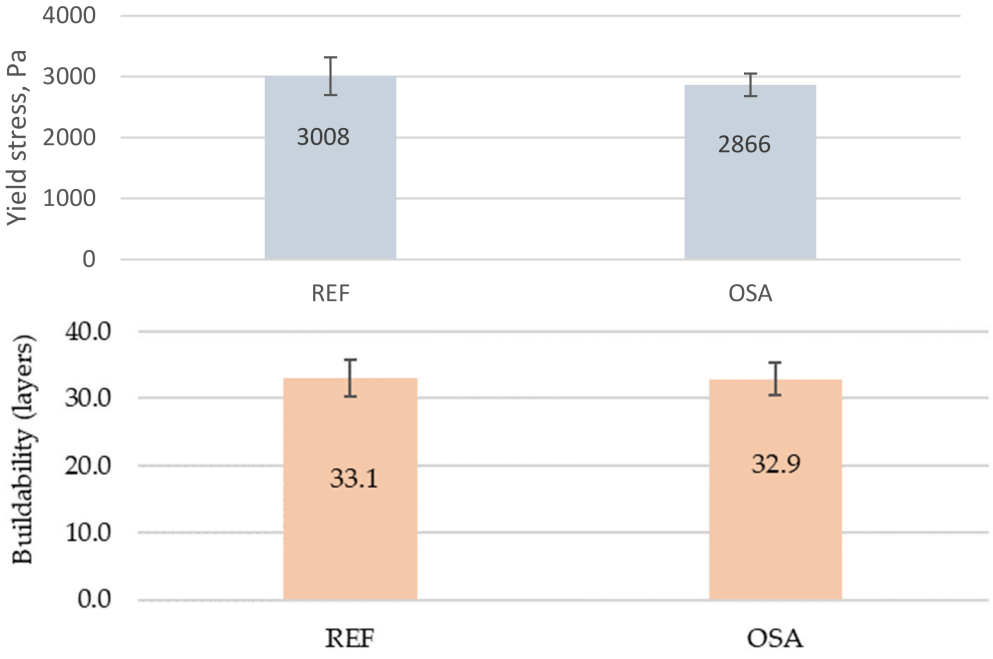
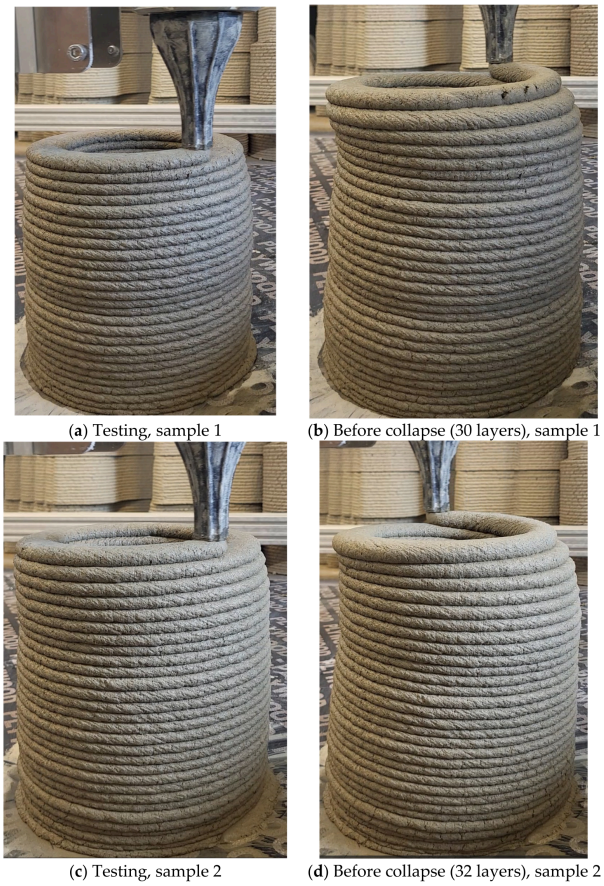


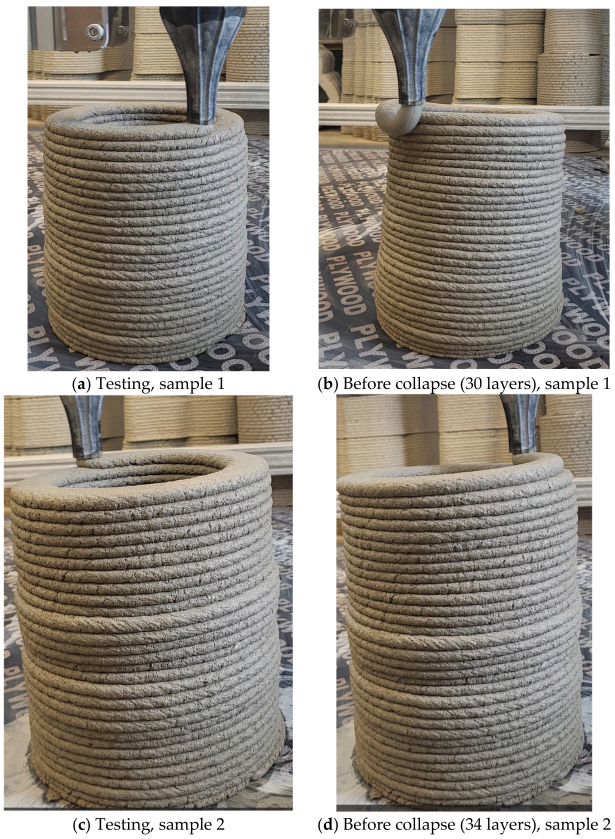
Figure 11. Yield stress by slug test (above) and buckling (buildability) test results for OSA and REF compositions.



(**a**) Testing, sample 1 (**b**) Before collapse (30 layers), sample 1

(**c**) Testing, sample 2 (**d**) Before collapse (32 layers), sample 2

Figure 12. Buildability test for REF composition, samples 1 (**a**,**b**) and 2 (**c**,**d**).



(**a**) Testing, sample 1 (**b**) Before collapse (30 layers), sample 1

(**c**) Testing, sample 2 (**d**) Before collapse (34 layers), sample 2

Figure 13. Buildability test for OSA composition, samples 1 (**a**,**b**) and 2 (**c**,**d**).

3.3. Density and Water Absorption

The results of determining the hardened material density of both compositions in wet condition are shown in Figure 14. As expected, no significant differences were observed in the 3D-printed and cast sample results. However, for cast samples the average density is 2070 and for 3D-printed ones 2058 kg/m^3. The minimal difference of 12 kg/m^3 can be explained by additional macroporosity that can be associated with entrapted air in the interlayer area in the 3D-printed block. It should also be noted that the average density of the fresh mixture is slightly less than the density of hardened concrete. This can be explained by the loss of entrained air during the 3D printing and sample production process. There are scientific studies that indicate changes in the pore system during extrusion-based 3D printing [41]. It can be argued that the results differ very slightly since the intervals of the standard deviations for all compositions overlap. The density of the fresh mixture has large variations in results, which can be explained by differences in the content of entrained air, the volume of which is difficult to control. According to the results of testing the fresh mixture, the volume of entrained air was initially between 9.5 and 12.5%.

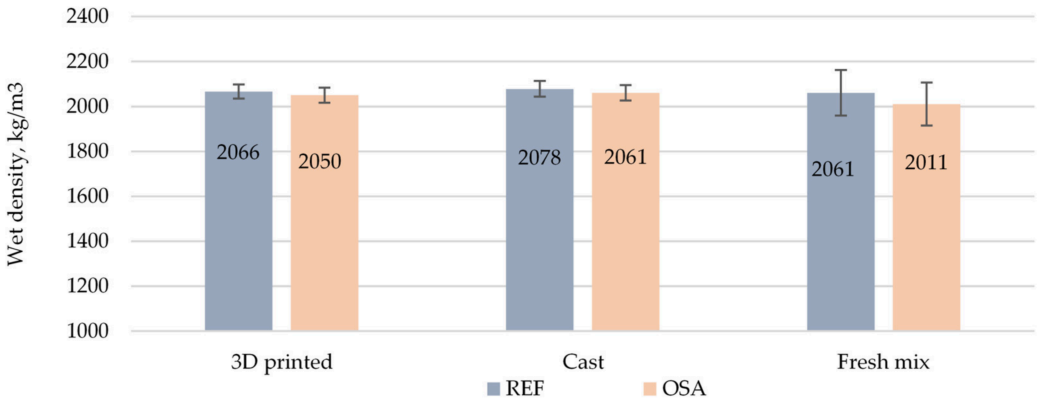


Figure 14. The results of material density.

The results of capillary water absorption and sorptivity index are summarised in Figures 15 and 16. Obtained results indicate that the 3D-printed samples exhibit approximately 20% higher water uptake than the cast samples, which is consistent with their slightly lower density. Also, 3D-printed compositions have an approximately 20% higher sorptivity index. This behaviour is attributed to the presence of interlayer interfaces and additional macro- and microporosity generated during the layer-by-layer deposition process, providing preferential pathways for moisture ingress. Similar results were observed in a previous study where the higher porosity of 3D-printed samples was explained by a more irregular 3D-printed surface and porosity in the interlayer region facilitating greater water penetration [30]. Sorptivity index results range from 0.10 to 0.13 kg/m^2/min$^{0.5}$. This is within the range of large-scale interlaboratory tests conducted within the RILEM ADC interlaboratory study [35]. Some studies report that the 3D-printing process influences concrete density and water absorption through its extrusion process and layer-by-layer deposition [42]. The extruded concrete could be denser than traditionally cast concrete, but the vulnerable interfaces between printed layers introduce higher localised porosity, accelerating water penetration. In the reviewed research [43], the authors applied 3D-printed and cast concrete analysis by re-structuring X-CT images. Nevertheless, despite the increased capillary absorption, the ternary OSA–MK composition demonstrated water absorption behaviour comparable to the reference mixture, indicating that the incorporation of oil shale ash and metakaolin did not adversely affect the overall pore structure.

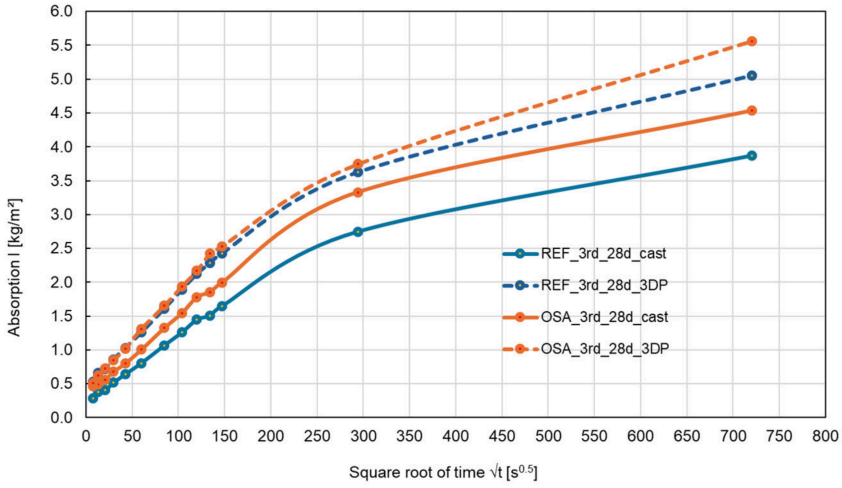


Figure 15. Surface capillary water absorption charts.

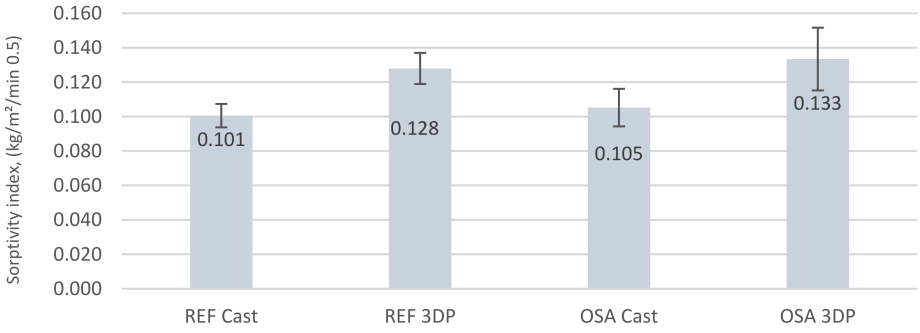


Figure 16. The values of the sorptivity index.

The pore structure of 3D-printed elements could be considered as comprising at least two relevant contributions: intrinsic matrix porosity, including capillary pores formed during hydration and drying, and 3D-printing-induced interfacial voids generated between consecutively deposited filaments. Therefore, adequate extrusion pressure and deformation of fresh filaments can produce dense interfaces and limit this effect. The water-absorption method used examines the combined contribution of accessible and interconnected pores, and the relative contribution of matrix and interlayer porosity cannot be distinguished quantitatively. However, matrix/capillary porosity and interlayer voids cannot be quantified separately by the absorption test.

3.4. Mechanical Strength

Mechanical tests were performed on cast and 3D-printed samples in a direction related to printing in accordance with Figure 4. Flexural and compressive test results are summarised in Figures 17 and 18 correspondingly.

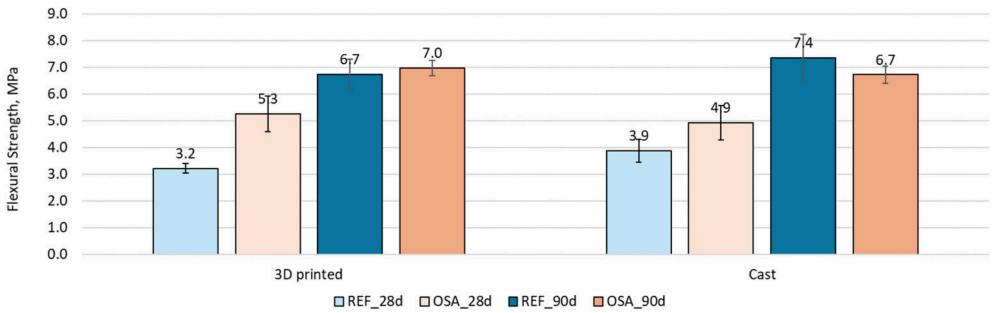


Figure 17. Flexural strength results in the v.u. direction of 3D-printed and cast samples.

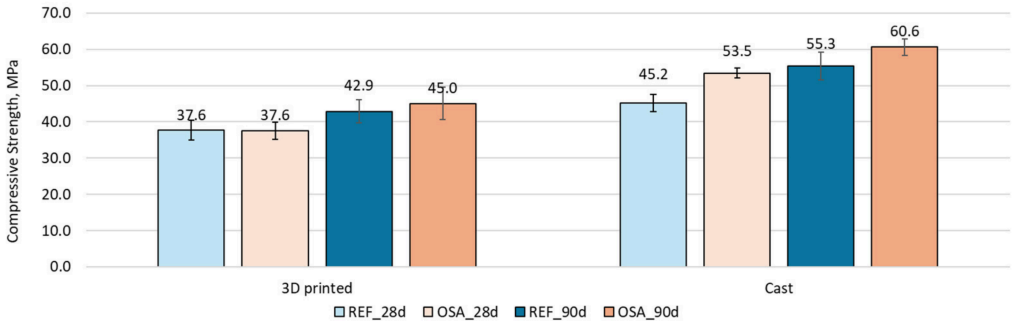


Figure 18. Compressive strength results in the w direction of 3D-printed and cast samples.

The test results obtained for 3D-printed samples tested in the v.u. flexural direction are consistent with the findings of the RILEM interlaboratory study [19], which identified this orientation as one of the most favourable loading configurations for 3D-printed concrete. In the v.u. direction, the principal tensile stresses develop predominantly parallel to the printed layers, so failure is governed by the strength of the cementitious matrix rather than by the weaker interlayer bond. Consequently, 3D printing itself does not reduce flexural strength in this orientation and may even provide a slight improvement through enhanced compaction during extrusion.

The incorporation of oil shale ash (OSA) had a much more pronounced effect than the manufacturing method. At 28 days, OSA increased the flexural strength from 3.2 to 5.3 MPa in the printed samples (approximately 66% increase) and from 3.9 to 4.9 MPa in the cast samples (approximately 26% increase). At 90 days, the OSA mixtures reached 7.0 MPa for the printed samples and 6.7 MPa for the cast samples. Compared with the corresponding reference mixtures, this represents a modest increase of about 4% for the printed samples, while the cast samples showed a slight decrease (about 9%), although the values remain within the experimental scatter indicated by the error bars.

The results also show that the 3D-printing process had only a limited influence on flexural performance in the v.u. direction (within the experimental scatter), which agrees well with the RILEM observations that this loading orientation is relatively insensitive to interlayer weakness.

The incorporation of OSA had a pronounced effect on 28-day flexural strength (Figure 17). For the 3D-printed specimens, flexural strength increased from 3.2 to 5.3 MPa, corresponding to an approximately 66% increase, which was statistically significant ($p = 0.0039$). For the cast specimens, OSA increased the strength from 3.9 to 4.9 MPa (approximately 26%), also representing a statistically significant difference ($p = 0.0073$). At 90 days, the differences between REF and OSA were considerably less and were not statistically significant for either printed ($p = 0.266$) or cast ($p = 0.203$) specimens. Comparison of manufacturing methods showed a significant difference between printed and cast REF specimens at 28 days ($p = 0.0417$), whereas the remaining cast and printed comparisons were not statistically significant ($p > 0.05$).

The compressive strength experimental results (Figure 18) show that the cast samples consistently achieved higher compressive strengths than the 3D-printed samples. At 28 days, the reference mixtures reached 37.6 MPa (3D printed) and 45.2 MPa (cast), while at 90 days their strengths increased to 42.9 MPa and 55.3 MPa, respectively. The replacement of PC with oil shale ash and metakaolin had a positive influence on the cast samples, achieving a maximal strength of 60.6 MPa at 90 days.

The compressive strength results obtained in the w direction agree with the findings of the RILEM interlaboratory study, which reported that samples loaded perpendicular to the printing plane generally exhibit slightly lower compressive strength than cast sam-

ples [20]. The compressive strength results (Figure 18) demonstrate a statistically significant influence of the manufacturing method. Cast specimens showed higher strength than the corresponding 3D-printed specimens for both REF and OSA compositions. At 28 days, the difference between cast and printed specimens was significant for REF ($p = 0.033$) and highly significant for OSA ($p < 0.001$). Similar differences were observed at 90 days ($p = 0.001$ for REF and $p < 0.001$ for OSA). In contrast, no statistically significant difference between REF and OSA was observed for 3D-printed specimens at either 28 days ($p = 1.000$) or 90 days ($p = 0.333$). For cast specimens, OSA resulted in significantly higher compressive strength than REF at both 28 days ($p = 0.024$) and 90 days ($p = 0.033$). The OSA printed specimens also exhibited a significant strength increase between 28 and 90 days ($p < 0.001$), indicating continued long-term strength development.

In this study, mechanical strength was evaluated at 28 and 90 days. Detailed early-age 3- and 7-day strength development and their relationship with early-age structure development and buildability remain subjects for further investigation.

3.5. Frost Resistance

Freeze–thaw resistance was evaluated according to slab method of a standard LVS CEN/TS 12390-9:2017 [44]. Samples were prepared, and four test series were evaluated: REF cast and 3D printed and OSA cast and 3D printed. Two types of tests were used: a standard slab test with one freeze–thaw cycle per day (test performed in KTU) and an accelerated test with two freeze–thaw cycles per day (test performed in RTU). In all cases, 56 freeze–thaw cycles were performed using a 3% sodium chloride solution as a freezing medium. Prepared cast and 3D-printed samples for frost resistance testing are shown in Figure 19.



Figure 19. Cast and 3D-printed samples for frost resistance testing.

The results of surface scaling are summarised in Figures 20 and 21. Comparison of numerical value of mass loss per unit area of concrete surface shows that the results differ significantly, especially for the two-cycle-per-day test (Figure 21). The results of a standard test (Figure 20, one cycle per day) show a mass loss value not exceeding 300 g/m^2, and the differences between the series do not exceed the values of standard deviations.

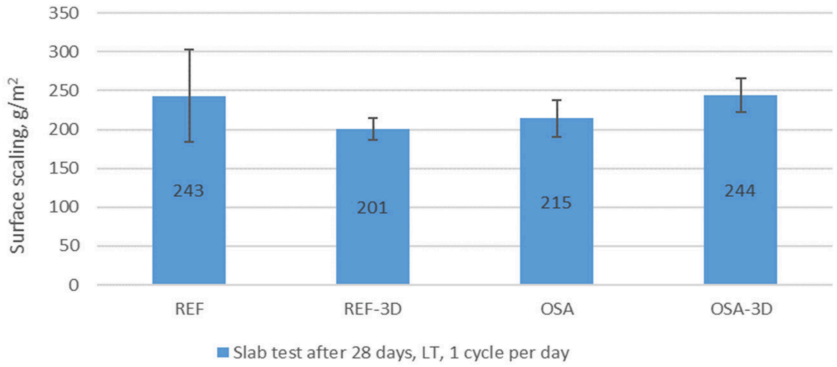


Figure 20. Frost resistance test results: slab test for 28-day-old samples, test performed in KTU, 1 cycle per day.

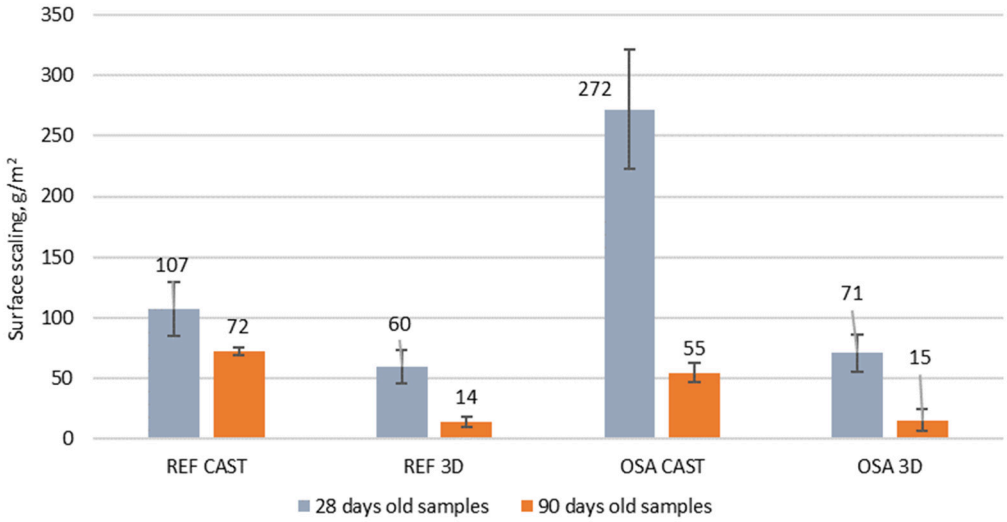


Figure 21. Frost resistance test results: slab test for 28- and 90-day-old samples, test performed in RTU, 2 cycles per day.

The freeze–thaw test results confirmed satisfactory durability of both the reference and OSA-based mixtures, with no evidence of critical surface deterioration after cyclic freezing. Although the 3D-printed samples showed slightly higher water absorption, this did not result in a significant reduction in frost resistance, suggesting that the pore system remained sufficiently stable to accommodate freezing-induced stresses. Moreover, the indicated mass losses are considered insignificant and in accordance with [45], corresponding to the highest quality assessment of concrete for frost resistance.

Analysis of the frost-resistance results obtained using two freeze–thaw cycles per day (Figure 21) showed lower surface mass loss than in the standard test, although greater variability was observed, particularly for the cast OSA specimens. The accelerated test was performed on specimens aged for 28 and 90 days. The 90-day specimens exhibited the lowest surface scaling, which may be attributed to further hydration and long-term pozzolanic reactions that progressively densified the concrete microstructure [46].

The freeze–thaw results indicate that 3D printing did not adversely affect the frost resistance of the investigated concrete mixtures. In both test methods, the 3D-printed reference samples exhibited equal or lower surface scaling than the corresponding cast samples, indicating comparable or slightly improved resistance to freeze–thaw damage. In the LT test (1 cycle/day), the surface scaling decreased from 243 to 201 g/m^2 for the reference mixture after 3D printing, while in the RTU test (two cycles/day) it decreased from 107 to 60 g/m^2. The incorporation of oil shale ash (OSA) did not show a detrimental effect

on frost resistance in the printed samples. In the LT test, the OSA mixture exhibited nearly identical surface scaling for cast and printed samples (215 and 244 g/m^2, respectively), while in the RTU test the 3D-printed OSA samples (71 g/m^2) showed substantially lower scaling than the cast OSA samples (272 g/m^2). The difference between cast and 3D-printed OSA specimens in the accelerated test results can be interpreted ambiguously. Since the standard test showed similar scaling values, the accelerated-test result could reflect experimental variability and differences in the near-surface structure of cast and printed specimens rather than an intrinsic improvement caused by 3D printing.

The Swedish standard SS 137244:2019 [47] summarises classification of the measured scaling. In accordance with this, the scaling below the 0.5 kg/m^2 corresponds to "good" frost resistance.

Although the 56-cycle test provides a standardised comparative assessment of freeze–thaw resistance, it does not reproduce the substantially larger number of cycles and combined environmental actions that may occur during long-term outdoor service. Therefore, extended cyclic testing and long-term field exposure are required to confirm the durability of the developed compositions under practical service conditions.

There are diverse results of frost resistance tests for 3D concrete in the scientific literature. Most studies report a decrease in strength and frost resistance due to increased porosity and defects in the interlayer space. However, some studies show equivalent frost resistance for 3D concrete and cast concrete. Despite these microstructural differences, the overall freeze–thaw performance of the investigated material remained comparable to cast concrete, indicating that well-printed concrete with limited interlayer defects can maintain satisfactory frost resistance. The relationship between pore structure and frost resistance is further supported by P. Sikora et al. (2022) [48]. Although freeze–thaw durability was not the primary focus of the study, the authors compared cast and printed concrete and found that three-layer printed samples possessed lower density and higher capillary porosity than cast samples.

The combined action of metakaolin-induced pozzolanic reactions and the air-entraining system likely contributed to refining the microstructure and improving resistance to freeze–thaw damage. The durability results demonstrate that replacing 40% of Portland cement with oil shale ash and metakaolin can produce a 3D-printable cementitious composite suitable for outdoor exposure. At the same time, the higher capillary absorption of printed elements indirectly highlights the influence of interlayer interfaces on moisture transport, emphasising that optimisation of the printing process remains important for maximising long-term durability.

Compared with fly ash- and slag-based printable materials (more widely studied), the developed OSA–MK system achieved 40% Portland-cement replacement while maintaining yield stress and buildability close to the reference mixture. The use of a compositions containing fly ash extended the opening time and did not significantly influence early structural build-up, whereas slag generally improves green strength but can shorten the printable window. The main advantages of the present OSA–MK system are stable printability and the development of long-term strength, while its main limitation is the variability of OSA composition and the need for further evaluation of early-age and interlayer-bond properties.

The OSA–MK composition investigated in this study was selected through preceding iterative mixture-development stages, in which different proportions and combinations of Portland cement, OSA and MK were evaluated in the frame of project transition. The present study focuses on industrial production and comprehensive evaluation of the selected composition rather than on optimisation of the OSA/MK ratio. Interlayer bond strength was not measured directly; the influence of interlayer interfaces was assessed indirectly through mechanical properties and capillary water absorption.

4. Conclusions

A sustainable low-cement 3D-printable cementitious composite was developed by replacing 40 wt.% of Portland cement with a ternary binder containing oil shale ash (OSA) and metakaolin (MK). The developed formulations were successfully transferred from laboratory scale to industrially manufactured pre-blended dry mixes by Sakret Latvia, demonstrating the feasibility of producing ready-to-use materials for additive manufacturing. PSD characterisation, fresh-state testing, and full-scale 3D-printing trials confirmed stable extrusion, good buildability, and reproducible printing performance.

Comprehensive characterisation of the raw materials confirmed the suitability of OSA as a supplementary cementitious material. The mineralogical characterisation confirmed that the selected raw materials provide a complementary ternary binder system suitable for low-cement 3D-printable composites. Chemical analysis showed that OSA contains 33.6% CaO, 28.6% SiO_2, and 10.5% Al_2O_3, while XRD identified an amorphous phase content of about 60%, indicating significant hydraulic and pozzolanic activity. Together with the high fineness of metakaolin (d_{50} = 6.5 μm), these characteristics promoted long-term hydration and matrix densification. XRD analysis of the industrially produced REF and OSA pre-blended dry mixes verified that the designed phase composition was successfully transferred to production scale, demonstrating the feasibility of manufacturing stable, ready-to-use dry products for extrusion-based 3D concrete printing.

Ternary binder shows no strength reduction at 28 days, and its compressive strength continued to increase and exceeded the reference mixture after 90 days. Mechanical testing confirmed the differences between cast and 3D-printed elements due to interlayer interfaces, while durability tests demonstrated satisfactory water absorption and freeze–thaw resistance for all tested samples. Surface scaling after 56 freeze–thaw cycles remained below approximately 300 g/m^2, indicating suitability for outdoor exposure. The results demonstrate that printed OSA performs comparably, whereas cast OSA shows the highest scaling under the accelerated test.

Durability testing demonstrated good resistance to freeze–thaw surface scaling. After 56 freeze–thaw cycles in the presence of 3% NaCl, cumulative surface scaling remained below approximately 300 g/m^2 for all investigated compositions. These values satisfy the criteria for "good" salt-frost scaling resistance according to SS 137244:2019.

Freeze–thaw testing indicated that 3D printing did not adversely affect the durability of the investigated compositions. The influence of OSA depends on the specimen preparation method and testing conditions: the printed OSA specimens showed freeze–thaw performance comparable to the reference composition, whereas the cast OSA specimens exhibited the highest surface scaling. These results indicate that the effect of OSA on freeze–thaw resistance should be interpreted with consideration of manufacturing method and exposure conditions.

The developed OSA–MK binder provides an environmentally friendly alternative for 3D concrete printing by significantly reducing cement consumption while maintaining good printability, mechanical performance, and durability. The successful industrial production of pre-blended dry mixes and their validation through laboratory and full-scale 3D-printing tests represent an important step toward the practical implementation of sustainable additive manufacturing in construction.

The comparison of cast and 3D-printed sample results indicate that the loading orientation (v.u.) effectively minimised the detrimental influence of layer interfaces, allowing the intrinsic material properties to dominate the flexural response. Under these conditions, the addition of oil shale ash was the primary factor controlling the improvement in flexural strength, particularly at early ages, while the difference between cast and 3D-printed samples remained comparatively small. 3D printing resulted in a moderate reduction in

compressive strength in the w direction, whereas oil shale ash contributed to improved long-term compressive strength, with the most pronounced effect observed in the cast samples. This behaviour is consistent with the general conclusion of the RILEM TC 304-ADC study that flexural strength reductions are mainly observed only when tensile stresses act perpendicular to the printed layers, whereas the v.u. orientation largely preserves the mechanical performance of printed concrete.

Author Contributions: Conceptualization, G.S. and M.S.; methodology, M.S., E.S. (Evaldas Serelis), G.S. and A.S.; validation, E.S. (Ella Spuriņa), V.Z.S. and A.S.; formal analysis, L.K.B.; investigation, A.S., E.S. (Evaldas Serelis), and E.S. (Ella Spuriņa); resources, M.S.; data curation, A.S. and E.S. (Ella Spuriņa); writing—original draft preparation, G.S.; writing—review and editing, M.S., V.Z.S., L.K.B. and G.S.; visualization, G.S. and A.S.; supervision, M.S. and L.H.; project administration, M.S. and L.K.B.; funding acquisition, L.H. and M.S. All authors have read and agreed to the published version of the manuscript.

Funding: This research was funded through the transnational M-ERA.NET Joint Call 2022, project title "Transforming waste into high-performance 3D printable cementitious composite", acronym: Transition, funding period 2023–2026, https://www.m-era.net/home (accessed on 29 December 2024). The authors acknowledge the Slovenian Research and Innovation Agency: research core funding No. P2-0273 and infrastructure programme No. I0-0032.

Data Availability Statement: The original contributions presented in this study are included in this article. Further inquiries can be directed to the corresponding author.

Acknowledgments: During the preparation of this study, the authors used Gemini 3.1. Pro for the purposes of text revision. The authors have reviewed and edited the output and take full responsibility for the content of this publication.

Conflicts of Interest: The authors declare no conflicts of interest.

Abbreviations

The following abbreviations are used in this manuscript:

OSA	Oil shale ash
3DCP	3D concrete printing
SCM	Supplementary cementitious material
XRD	X-ray diffraction
MK	Metakaolin
SEM	Scanning electron microscope
PSD	Particle size distribution
SP	Superplasticizer
AEA	Air-entraining agent
VMA	Viscosity-modifying additive
PP	Polypropylene micro-fibre

References

1. Buswell, R.A.; Leal de Silva, W.R.; Jones, S.Z.; Dirrenberger, J. 3D Printing Using Concrete Extrusion: A Roadmap for Research. *Cem. Concr. Res.* **2018**, *112*, 37–49. [CrossRef]
2. Tay, Y.W.D.; Panda, B.; Paul, S.C.; Noor Mohamed, N.A.; Tan, M.J.; Leong, K.F. 3D Printing Trends in Building and Construction Industry: A Review. *Virtual Phys. Prototyp.* **2017**, *12*, 261–276. [CrossRef]
3. Wangler, T.; Lloret, E.; Reiter, L.; Hack, N.; Gramazio, F.; Kohler, M.; Bernhard, M.; Dillenburger, B.; Buchli, J.; Roussel, N.; et al. Digital Concrete: Opportunities and Challenges. *RILEM Tech. Lett.* **2016**, *1*, 67–75. [CrossRef]
4. Panda, B.; Tay, Y.W.D.; Paul, S.C.; Tan, M.J. Current Challenges and Future Potential of 3D Concrete Printing. *Materwiss. Werksttech.* **2018**, *49*, 666–673. [CrossRef]
5. Panda, B.; Mohamed, N.A.N.; Paul, S.C.; Singh, G.V.P.B.; Tan, M.J.; Šavija, B. The Effect of Material Fresh Properties and Process Parameters on Buildability and Interlayer Adhesion of 3D Printed Concrete. *Materials* **2019**, *12*, 2149. [CrossRef] [PubMed]

6. Uibu, M.; Tamm, K.; Viires, R.; Reinik, J.; Somelar, P.; Raado, L.; Hain, T.; Kuusik, R.; Trikkel, A. The Composition and Properties of Ash in the Context of the Modernisation of Oil Shale Industry. *Oil Shale* **2021**, *38*, 155–176. [CrossRef]
7. Uibu, M.; Somelar, P.; Raado, L.M.; Irha, N.; Hain, T.; Koroljova, A.; Kuusik, R. Oil Shale Ash Based Backfilling Concrete—Strength Development, Mineral Transformations and Leachability. *Constr. Build. Mater.* **2016**, *102*, 620–630. [CrossRef]
8. Kalpokaitė-Dičkuvienė, R.; Pitak, I.; Baltušnikas, A.; Čėsnienė, J.; Kriūkienė, R.; Lukošiūtė, S.I. Functional and Microstructural Alterations in Hydrated and Freeze–Thawed Cement-Oil Shale Ash Composites. *Case Stud. Constr. Mater.* **2023**, *19*, e02302. [CrossRef]
9. Le, T.T.; Austin, S.A.; Lim, S.; Buswell, R.A.; Gibb, A.G.F.; Thorpe, T. Mix Design and Fresh Properties for High-Performance Printing Concrete. *Mater. Struct.* **2012**, *45*, 1221–1232. [CrossRef]
10. Haddad, R.H.; Ashteyat, A.M.; Lababneh, Z.K. Producing Geopolymer Composites Using Oil Shale Ash. *Struct. Concr.* **2019**, *20*, 225–235. [CrossRef]
11. Panda, B.; Paul, S.C.; Mohamed, N.A.N.; Tay, Y.W.D.; Tan, M.J. Measurement of Tensile Bond Strength of 3D Printed Geopolymer Mortar. *Measurement* **2018**, *113*, 108–116. [CrossRef]
12. Sapata, A.; Šinka, M.; Šahmenko, G.; Bajare, D.; Migliniece, B.; Hanzic, L.; Štefancic, M. Development of 3D Printable Cement-Based Composite Containing Oil Shale Ash. In Proceedings of the Digital Concrete 2024—Supplementary Proceedings, Munich, Germany, 4–6 September 2024.
13. Samrani, P.; Cao, Y.; Fimbres-Weihs, G.; Sanjaya, E.; Abbas, A. Effect of Fly Ash and Ground Waste Glass as Cement Replacement in Concrete 3D-Printing for Sustainable Construction. *Front. Built Environ.* **2024**, *10*, 1430174. [CrossRef]
14. Al-Noaimat, Y.A.; Ghaffar, S.H.; Chougan, M.; Al-Kheetan, M.J. A Review of 3D Printing Low-Carbon Concrete with One-Part Geopolymer: Engineering, Environmental and Economic Feasibility. *Case Stud. Constr. Mater.* **2023**, *18*, e01818. [CrossRef]
15. Ye, J.; Teng, F.; Yu, J.; Yu, S.; Du, H.; Zhang, D.; Ruan, S.; Weng, Y. Development of 3D Printable Engineered Cementitious Composites with Incineration Bottom Ash (IBA) for Sustainable and Digital Construction. *J. Clean. Prod.* **2023**, *422*, 138639. [CrossRef]
16. Li, Z.; Hojati, M.; Wu, Z.; Piasente, J.; Ashrafi, N.; Duarte, J.P.; Nazarian, S.; Bilén, S.G.; Memari, A.M.; Radlińska, A. Fresh and Hardened Properties of Extrusion-Based 3D-Printed Cementitious Materials: A Review. *Sustainability* **2020**, *12*, 5628. [CrossRef]
17. Zhang, G.; Li, J.; Wang, H.; Shangguan, C.; Xie, J.; Zhou, Y. Research on the Impact Toughness of 3D-Printed CoCrMo Alloy Components Based on Fractal Theory. *Biomimetics* **2025**, *10*, 292. [CrossRef] [PubMed]
18. Bos, F.; Menna, C.; Robens-Radermacher, A.; Wolfs, R.; Roussel, N.; Lombois-Burger, H.; Baz, B.; Weger, D.; Nematollahi, B.; Santhanam, M.; et al. Mechanical Properties of 3D Printed Concrete: A RILEM TC 304-ADC Interlaboratory Study—Approach and Main Results. *Mater. Struct.* **2025**, *58*, 183. [CrossRef]
19. Wolfs, R.; Versteege, J.; Santhanam, M.; Bhattacherjee, S.; Bos, F.; Robens-Radermacher, A.; Muthukrishnan, S.; Menna, C.; Ozturk, O.; Ozyurt, N.; et al. Mechanical Properties of 3D Printed Concrete: A RILEM TC 304-ADC Interlaboratory Study—Flexural and Tensile Strength. *Mater. Struct.* **2025**, *58*, 182. [CrossRef]
20. Mechtcherine, V.; Muthukrishnan, S.; Robens-Radermacher, A.; Wolfs, R.; Versteege, J.; Menna, C.; Ozturk, O.; Ozyurt, N.; Roupec, J.; Richter, C.; et al. Mechanical Properties of 3D Printed Concrete: A RILEM 304-ADC Interlaboratory Study—Compressive Strength and Modulus of Elasticity. *Mater. Struct.* **2025**, *58*, 181. [CrossRef]
21. *EN 197-1:2011*; Cement—Part 1: Composition, Specifications and Conformity Criteria for Common Cements. European Committee for Standardization (CEN): Brussels, Belgium, 2011.
22. Žvironaite, J.; Kligys, M.; Pundiene, I.; Pranckevičiene, J. Effect of Limestone Particles on Rheological Properties and Hardening Process of Plasticized Cement Pastes. *Medziagotyra* **2015**, *21*, 143–148. [CrossRef]
23. Hanžič, L.; Štefančič, M.; Šter, K.; Zalar Serjun, V.; Šinka, M.; Sapata, A.; Šahmenko, G.; Šerelis, E.; Migliniece, B.; Korat Bensa, L. Collision Milling of Oil Shale Ash as Constituent Pretreatment in Concrete 3D Printing. *Infrastructures* **2025**, *10*, 18. [CrossRef]
24. Srivastava, V.; Kumar, R.; Agarwal, V.C. Metakaolin Inclusion: Effect on Mechanical Properties of Concrete. *J. Acad. Indus. Res.* **2012**, *1*, 251–253.
25. Guemmadi, Z.; Resheidat, M.; Chabil, H.; Toumi, B. Modeling the Influence of Limestone Filler on Concrete: A Novel Approach for Strength and Cost. *Jordan J. Civ. Eng.* **2009**, *3*, 158–171.
26. Hou, S.; Duan, Z.; Xiao, J.; Ye, J. A Review of 3D Printed Concrete: Performance Requirements, Testing Measurements and Mix Design. *Constr. Build. Mater.* **2021**, *273*, 121745. [CrossRef]
27. Akhlaghi, O.; Aytas, T.; Tatli, B.; Sezer, D.; Hodaei, A.; Favier, A.; Scrivener, K.; Menceloglu, Y.Z.; Akbulut, O. Modified Poly(Carboxylate Ether)-Based Superplasticizer for Enhanced Flowability of Calcined Clay-Limestone-Gypsum Blended Portland Cement. *Cem. Concr. Res.* **2017**, *101*, 114–122. [CrossRef]
28. Song, H.; Park, J. The Effects of 3D Printing on Frost Resistance of Concrete The Effects of 3D Printing on Frost Resistance of Concrete. *J. Phys. Conf. Ser.* **2023**, *2423*, 012037. [CrossRef]
29. Łaźniewska-Piekarczyk, B. The influence of the type of low-emission cement and air-entraining admixtures on the quality of air entrainment of concrete—Unexpected impact of granulated blast furnace slag. *Struct. Environ.* **2024**, *16*, 222–232. [CrossRef]

30. Sapata, A.; Šinka, M.; Šahmenko, G.; Korat Bensa, L.; Hanžič, L.; Šter, K.; Ručevskis, S.; Bajāre, D.; Bos, F.P. Establishing Benchmark Properties for 3D-Printed Concrete: A Study of Printability, Strength, and Durability. *J. Compos. Sci.* **2025**, *9*, 74. [CrossRef]
31. *EN 1015-3:1999/A1:2004/A2:2006*; Methods of Test for Mortar for Masonry—Part 3: Determination of Consistence of Fresh Mortar (by Flow Table). European Committee for Standardization (CEN): Brussels, Belgium, 2006.
32. Puzule, L.; Spurina, E.; Frolovs, G.; Dragons, D.; Dias, A.C.; Sinka, M. 3D Printing of Bio-Based Building Materials—Mix Design, Properties and CO_2 Footprint Assessment. *Case Stud. Constr. Mater.* **2026**, *25*, e06444. [CrossRef]
33. Ducoulombier, N.; Mesnil, R.; Carneau, P.; Demont, L.; Bessaies-Bey, H.; Caron, J.F.; Roussel, N. The "Slugs-Test" for Extrusion-Based Additive Manufacturing: Protocol, Analysis and Practical Limits. *Cem. Concr. Compos.* **2021**, *121*, 104074. [CrossRef]
34. *EN 196-1*; Methods of Testing Cement—Part 1: Determination of Strength. European Committee for Standardization: Brussels, Belgium, 2016.
35. Zhang, Y.; de Lima, L.N.; Böhler, D.; Arunothayan, A.; Babafemi, A.J.; Baz, B.; Caneda-Martinez, L.; De Schutter, G.; Du, H.; Freund, N.; et al. Durability assessment of 3D printed cement-based materials: A RILEM TC 304-ADC interlaboratory study. *Mater. Struct.* **2025**, *58*, 314. [CrossRef]
36. *ISO 13320:2020*; Particle Size Analysis—Laser Diffraction Methods. International Organization for Standardization (ISO): Geneva, Switzerland, 2020.
37. Weng, Y.; Li, M.; Tan, M.J.; Qian, S. Design 3D Printing Cementitious Materials via Fuller Thompson Theory and Marson-Percy Model. *Constr. Build. Mater.* **2018**, *163*, 600–610. [CrossRef]
38. Sahmenko, G.; Rucevskis, S.; Lusis, V.; Spure, L.; Korjakins, A.; Annamaneni, K.K.; Bajare, D. Elaboration Mix Design Methodology for Obtaining Defined Properties of Cement Composite with Fly Ash, Silica Fume and Colloidal Silica. *Mech. Compos. Mater.* **2024**, *60*, 919–938. [CrossRef]
39. Oymael, S. Suitability of oil shale ash as a constituent of cement. *Oil Shale* **2007**, *24*, 45–58. [CrossRef]
40. Jayathilakage, R.; Rajeev, P.; Sanjayan, J. Yield Stress Criteria to Assess the Buildability of 3D Concrete Printing. *Constr. Build. Mater.* **2020**, *240*, 117989. [CrossRef]
41. Das, A.; Song, Y.; Mantellato, S.; Wangler, T.; Lange, D.A.; Flatt, R.J. Effect of Processing on the Air Void System of 3D Printed Concrete. *Cem. Concr. Res.* **2022**, *156*, 106789. [CrossRef]
42. van den Heever, M.; du Plessis, A.; Kruger, J.; van Zijl, G. Evaluating the Effects of Porosity on the Mechanical Properties of Extrusion-Based 3D Printed Concrete. *Cem. Concr. Res.* **2022**, *153*, 106695. [CrossRef]
43. Zhang, Y.; Zhang, Y.; Yang, L.; Liu, G.; Du, H. Influence of the Pore Feature on the Water Uptake in 3D Printed Concrete. *Mater. Lett.* **2023**, *333*, 133642. [CrossRef]
44. *LVS CEN/TS 12390-9:2017*; Testing Hardened Concrete—Part 9: Freeze-Thaw Resistance with De-Icing Salts—Scaling. Latvian Standard (LVS): Riga, Latvia, 2017.
45. Piotrowski, T.; Jackiewicz-Rek, W.; Prochon, P.; Jeanpierre, A. Special Requirements for Freeze-Thaw Resistance of Concrete in PWR Nuclear Civil Works. *Mater. Bud.* **2016**, *529*, 94–97. [CrossRef]
46. Setina, J.; Gabrene, A.; Juhnevica, I. Effect of Pozzolanic Additives on Structure and Chemical Durability of Concrete. *Procedia Eng.* **2013**, *57*, 1005–1012. [CrossRef]
47. *SS 137244:2019*; Concrete Testing—Hardened Concrete—Scaling at Freezing. Swedish Institute for Standards (SIS): Stockholm, Sweden, 2019.
48. Sikora, P.; Techman, M.; Federowicz, K.; El-Khayatt, A.M.; Saudi, H.A.; Abd Elrahman, M.; Hoffmann, M.; Stephan, D.; Chung, S.Y. Insight into the Microstructural and Durability Characteristics of 3D Printed Concrete: Cast versus Printed Specimens. *Case Stud. Constr. Mater.* **2022**, *17*, e01320. [CrossRef]

Disclaimer/Publisher's Note: The statements, opinions and data contained in all publications are solely those of the individual author(s) and contributor(s) and not of MDPI and/or the editor(s). MDPI and/or the editor(s) disclaim responsibility for any injury to people or property resulting from any ideas, methods, instructions or products referred to in the content.